

Chapter 7

ULTRAFAST STRUCTURAL CHANGES INDUCED BY FEMTOSECOND LASER PULSES

H.O. Jeschke

Department of Physics and Astronomy, Rutgers University, 136 Frelinghuysen Road, Piscataway, NJ 08854-8019, USA

jeschke@physics.rutgers.edu

M.E. Garcia

Institut für Theoretische Physik der Freien Universität Berlin, Arnimallee 14, 14195 Berlin, Germany

garcia@physik.fu-berlin.de

Abstract A theoretical approach to treat laser induced femtosecond structural changes in covalent solids is described. Our approach consists in molecular dynamic simulations performed on the basis of a time-dependent, many-body potential energy surface derived from a tight-binding Hamiltonian. The shape and spectral composition of the laser pulse is explicitly taken into account in a non-perturbative way. We show a few examples of the application of this approach to describe the laser excitation of bulk diamond and ultrathin graphite and silicon films.

1. Introduction

The interaction of femtosecond laser pulses and solids gives rise to a large variety of novel and interesting effects. An important part of the laser induced ultrafast phenomena observed recently is concerned with structural changes. Laser pulses of durations ranging from a few femtoseconds up to half a picosecond and intensities above 10^{12} W/cm² may induce lattice instabilities which lead to thermal and nonthermal structural changes.

In the last years different types of laser induced ultrafast structure effects were observed, like excitation of coherent phonons [154, 155, 156, 157, 158] or nonequilibrium phase transitions, the latter including order-disorder [159, 160], solid-solid [161, 162] and solid-liquid [163, 164, 165, 166, 167, 157, 168, 169,

158, 170, 171] transformations. While the first experimental studies were based on optical methods (measurement of the reflectivity or dielectric function), several interesting x-ray experiments have been recently performed to analyze laser induced melting and crystalline-crystalline structural changes. In most experiments the rocking curves (changes in time of the Bragg angle) were measured [157, 168, 169, 158, 170, 171]. All these results show clear evidences of nonthermal structural changes.

Regarding the systems studied experimentally, a group of materials that merit particular attention are semiconductors because of their technological significance. Of special interest are materials like silicon (Si) and gallium arsenide (GaAs) which are widely used in semiconductor devices; here short time behavior becomes ever more important as the frequencies at which these devices are operated increase [172, 167]. The study of electronic relaxation time scales is very important for the development of nanodevices. A semimetal like germanium-doped antimony (GeSb) or carbon nanotubes are likely candidates for future technological applications like ultrafast optical storage media or cluster assembled materials [173, 174]. Finally, covalent solids like diamond, graphite and other carbon materials like DLC are of enormous technological interest because of their physical properties including extreme hardness and very high thermal conductivity. For these materials there is a large field of research concerning ultrashort laser-induced modification, annealing, ablation and machining [175].

Covalent systems are also interesting from the viewpoint of basic research, since their structural response differs dramatically from that of metals. For low or moderate laser pulse intensities, the different processes which take place during and after excitation of metals can be described by a simple physical picture, sketched in Fig. 7.1.

The femtosecond pulse creates hot electrons, which transfer their energy to the lattice via electron-phonon coupling and to the environment via diffusion. No laser induced bond breaking occurs. These processes are well described by the well known two-temperature model [176], which consists of a system of coupled differential equations for the electronic temperature $T_{el}(t)$ and the lattice temperature $T_{lattice}(t)$. Equilibrium parameters, like the lattice and electron specific heats, are included in the model. In contrast to the rather simple case of metals the femtosecond laser excitation of covalent solids exhibits new and interesting features. First, absorption of photons in covalent solids leads rapidly to bond-breaking processes. As soon as bonds are broken, the picture of electron-phonon coupling is no longer valid. Moreover, the concept of phonons becomes meaningless, since the potential landscape cannot be represented any more by a superposition of harmonic potentials. As a consequence, the two-temperature model breaks down and a different theoretical approach is necessary. Such an approach must take into account explicitly the atomic coor-

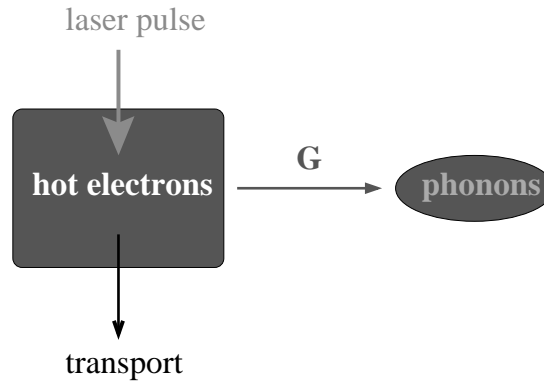


Figure 7.1: Schematic illustration of the processes taking place upon laser excitation of metals for low laser intensities. These processes can be well described by the two-temperature model.

dinates and must yield a correct description of the bonding. In this chapter we will describe in detail a microscopic theory for laser induced structural changes in covalent solids.

Good candidates for exhibiting interesting properties upon laser excitation are the different solid phases of Carbon, described in detail by Bundy *et al.* [175]. The open questions related to the phase diagram are still of fundamental interest. In particular, the question of whether several distinct liquid phases of carbon exist [177, 178], and if these phases can be induced by laser pulses attracts considerable attention.

Despite the intense experimental activities, only a few theoretical methods were derived in the last years to describe laser induced structural changes. Theoretical descriptions of laser induced structural changes in the different systems under experimental study like metals, covalent solids and ionic crystals are needed which are able to predict the effect of the influence of pulse duration and intensity on the lattice dynamics. As mentioned above, this chapter will deal with a complete theoretical description for the case of covalent solids.

In the literature, different theoretical approaches to the response of covalent solids to strong laser excitation can be found, which we mention in the following. P. Stampfli *et al.* [179, 180, 181] studied for the first time laser-induced lattice instabilities in Si, Ge and C. They analyzed the instability caused by the electron hole plasma in terms of one or two phonon degrees of freedom, and assuming that the density of the excited material remains constant during and after laser heating. This method can only give insight into the first femtoseconds after the laser pulse. By assuming the instant creation of an electron-hole plasma of a given density ξ at a time $t = 0$, the duration of the laser pulse is set to zero ($\tau = 0$). Herrmann, Gerlach and Campbell [182] have performed MD

simulations of the laser ablation of silicon. They use modified Stillinger-Weber potentials to model the interaction between the atoms. As we show in section 2, the use of model interatomic potentials which do not include the electrons as degrees of freedom do not allow for a theoretical treatment of laser induced structural changes.

Parrinello and coworkers employed first principles MD simulations [183, 184, 185]. These are based upon a treatment of the electrons and ions in the lattice with density functional theory in the local density approximation and with plane waves as basis functions. The volume of the MD cell was kept constant. The numerical cost of such calculations is very high [185], so that these methods would not permit a study of many different laser intensities and durations on various materials as was the intention of this work. Concerning the results obtained for the laser melting of silicon and graphite, respectively [184, 186], it seems possible that the choice of a constant volume MD method imposed too severe a restriction on the relaxation channels available to the material. Likewise, the results of a study of the liquid state of carbon [183] should be quite sensitive to the density, and thus a calculation at constant (graphitic) density might not answer all questions on the nature of molten carbon. Following Stampfli et al., these authors also assume for their melting studies the instant creation of a high electron temperature T_e at a time $t = 0$. Thus, the laser pulses are taken to be delta functions of duration $\tau = 0$ which makes it impossible to analyze the influence of the pulse duration. A similar approach as the one described above, but using a tight-binding basis instead of Kohn-Sham functions has been used by K. M. Ho and coworkers [187].

The method which will be presented in the next section was developed by us to study laser excitation of diamond, graphite, C_{60} -crystal and silicon in the bulk [161, 188, 189, 190, 191] and in ultrathin films [192, 193], and of C_{60} clusters [194].

Independently of our studies, R. Allen and coworkers developed a similar method to describe the excitation of coherent phonons and laser induced melting [195, 196, 197, 198]. This method is suitable for the study of the first few femtoseconds after excitation, since the assumption of constant volume is made and it is assumed that the electronic system does not undergo decoherence and thermalization processes after laser excitation.

The aim of our investigations is to understand on which time scale do laser-induced structural transitions occur, which relaxation channels are present and whether these relaxation channels be controlled by laser parameters like intensity, duration, and light frequency.

An important question which we attempt to answer is if there are fundamental differences between laser-induced and thermally induced bond breaking and phase transitions.

Important aspects taken into account in our theory are:

- (a) the admission of all relaxation channels in the response to an electron-hole plasma, including the calculation for all degrees of freedom and the admission of changes in sample volume and geometry,
- (b) the handling of the electronic nonequilibrium caused by strong laser excitation and its subsequent equilibration and relaxation, and
- (c) the treatment of laser pulses with finite durations $\tau > 0$.

The following section gives a brief account of the method applied in this work which will show how these extensions of previous theoretical work will be performed.

2. Theory

Our model for the femtosecond laser excitation of covalent solid is based on the following physical picture. Since light couples primarily with the electronic system, a laser pulse of moderate intensity produces the excitation of electrons from occupied to unoccupied levels. This creation of electron-hole pairs occurs with a time-dependent probability which is proportional to the (time-dependent) intensity of the laser field. As a consequence of the extremely fast excitation process, a nonequilibrium distribution of electrons is created. Through electron-electron collisions this electron distribution thermalizes to an equilibrium (Fermi-like) occupation of the electronic levels. Parallel to this electron thermalization process, hot electron transport from the excited region into the rest of the material sets in. During this complex electron dynamics the lattice does not remain frozen, but might undergo bond breaking and restructuring processes. These structural changes may lead to another crystal phase, to melting or to ablation. We show in this section that the reason why the lattice structure undergoes changes upon laser heating is related to the rapid and nonadiabatic change in time of the potential energy landscape $U(\{\mathbf{r}_{ij}\}, t)$ of the system when a large fraction of the electrons is excited. Note, that $U(\{\mathbf{r}_{ij}\}, t)$ is usually a very complex function of the interatomic distances $\mathbf{r}_{ij} = |\mathbf{r}_i - \mathbf{r}_j|$ and, for most materials, cannot be written as a sum of pair potentials.

We describe laser induced structural changes with the help of molecular dynamics simulations (MD). This means, that we treat the nuclear degrees of freedom of the problem classically. However, the electron dynamics must be treated quantum mechanically. The forces acting on the atoms are obtained as $\mathbf{F}_i(t) = -\vec{\nabla}_i U(\{\mathbf{r}_{ij}\}, t)$ and cause the lattice dynamics, described by Newton's equations of motion.

As mentioned in the previous section, special attention has to be given to the choice of the external parameters under which the MD simulations are performed. Simulations at constant volume would not be able to describe laser induced structural transformations involving density changes. The assumption

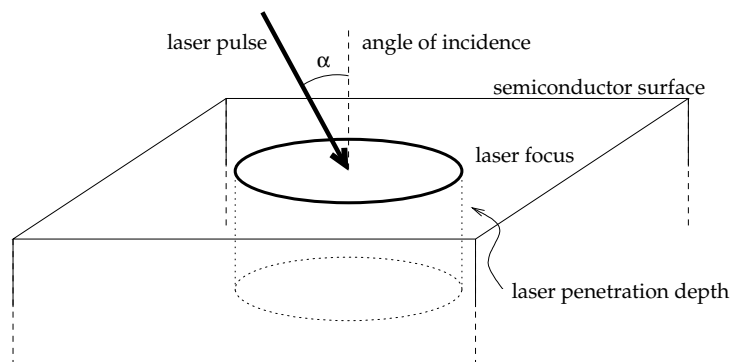


Figure 7.2: Sketch of the geometry of a laser pulse acting upon a solid surface. Note that this figure does not show the length scales in proportion; see text for dimensions.

of constant volume would artificially suppress such relaxation channels and would not describe correctly the laser heating process.

It is known [199] that the laser excited material reacts by a very fast expansion, which will be stronger in areas that have absorbed more laser energy; the laser intensity distribution can be expected to be Gaussian in space [200]. Thus, a surface profile as shown schematically in Fig. 7.2 is possible after a few picoseconds. For this reason, one possible approach to describe the situation is to make the volume and shape of the MD supercell variable, depending on the forces that prevail within. On the other hand, the considered MD supercell will because of its small extensions be surrounded by material that is subject to approximately the same degree of excitation. Therefore, locally a translation invariance is existent that is the prerequisite for the use of periodic boundary conditions.

Basically, we consider two different MD approaches, which will now be explained in some detail.

2.1 Lattice motion: molecular dynamics simulations

When we deal with the situation of an ultrafast laser pulse impinging on the surface of a semi-infinite solid, the geometry is as shown in Fig. 7.2. The typical lateral extension of the laser spot is $15 \mu\text{m}$ [165] and the penetration depth of the laser light is of the order of 100 nm , depending, of course, on the material and the frequency of the laser pulse. Consequently, the volume of the material excited by the laser is approximately $7 \times 10^{13} \text{ \AA}^3$, while the volume of a typical MD supercell is $\Omega = 10^3 \text{ \AA}^3$. Thus, the theory presented here can only deal with a very small sector of the entire system of laser excited material plus surrounding cold lattice. Taking this into account, we perform the following

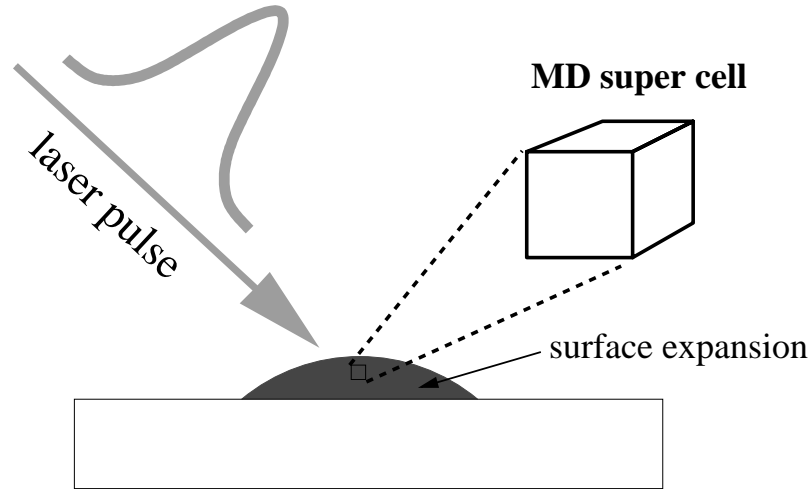


Figure 7.3: Illustration of the model used for the MD supercell to describe the time evolution of a piece of bulk solid upon laser excitation. The laser excited region of the covalent material expands into the vacuum due to femtosecond laser heating. We place the MD supercell inside the expanding region and use periodic boundary conditions in all three directions, simulating a small region of translational invariance. Shape and size changes of the MD supercell are permitted.

MD studies:

(i) We consider a subregion of volume $\Omega_{MD} \sim 10^3 \text{ \AA}^3$, represented by a MD supercell with periodic boundary conditions all directions, inside the much larger irradiated volume ($\Omega_{irr} \sim 10^{13} \text{ \AA}^3$). Fig. 7.3 shows schematically where the MD cell is placed and which part of the whole system it represents. Clearly, the cell is expected to undergo homogeneous rapid volume and shape changes upon laser heating. The only constraint acting on the MD cell is the external pressure on the solid, which remains constant.

(ii) We consider ultrathin films made out of a few number of layers. In this case, as shown in Fig. 7.4, the system can be described by a MD supercell which is periodically continued in the horizontal directions. The MD cell is rigid in order to account for the inertial confinement. However, it contains vacuum above and below the material, so that expansion of the system in the vertical direction is allowed. No assumptions on the external pressure are made.

Both techniques (i) and (ii) can be mathematically formulated as follows.

(i) Variable MD cell inside the heated region (bulk). We perform simulations at constant pressure [201, 202], which are based upon a Lagrangian of

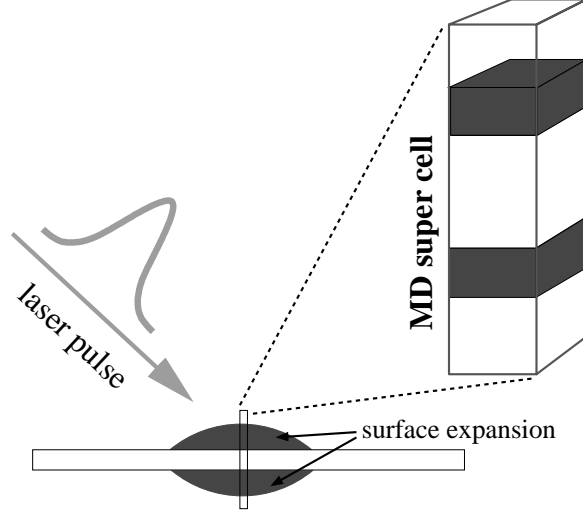


Figure 7.4: Modeling of the MD supercell for femtosecond laser heating of a thin film. The laser excited film expands into the vacuum on both sides. The MD supercell contains vacuum above and below the film in order to allow for an unhindered expansion perpendicular to the film. In the direction perpendicular to the surface, periodic boundary conditions are assumed.

the form

$$L(t) = \sum_{i=1}^N \frac{m_i}{2} \dot{\mathbf{s}}_i^T h^T h \dot{\mathbf{s}}_i + K_{cell} - U(\{r_{ij}\}, t) - P\Omega. \quad (7.1)$$

Here, the coordinates \mathbf{s}_i of the N atoms are taken relative to the vectors \mathbf{a} , \mathbf{b} and \mathbf{c} that form the MD supercell and constitute the matrix $h = (\mathbf{a} \ \mathbf{b} \ \mathbf{c})$. Note that the primitive vectors \mathbf{a} , \mathbf{b} and \mathbf{c} can move as a consequence of the laser excitation, changing the shape and the volume of the MD cell. The absolute coordinates of the atoms are obtained from $\mathbf{r}_i = h\mathbf{s}_i$. The volume of the MD cell, which is allowed to change in time is given by $\Omega = \det(h)$, and P is the external pressure, which remains constant. The first term of the Lagrangian accounts for the kinetic energy arising from the motion of the N atoms relative to the MD cell. The superscript T denotes the transposition of cell matrix h and relative velocity vectors $\dot{\mathbf{s}}_i$. The second term (K_{cell}) represents the contribution of the motion of the primitive vectors, i.e., the time-dependent shape changes of the MD cell, to the kinetic energy of the system [201, 202, 203]. There are different approximations for K_{cell} , which will be discussed below. The third term represents the potential energy surface $U(\{r_{ij}\}, t)$, which is determined from a microscopic theory as described below. The quantities r_{ij} are the interatomic distances. Note that, since periodic boundary conditions are assumed

in all directions, the interatomic distances are calculated as

$$r_{ij} = \sqrt{[h(\mathbf{s}_i - \mathbf{s}_j + \mathbf{z})]^2}, \quad z_\alpha \in \{-1, 0, 1\}. \quad (7.2)$$

Using the Euler-Lagrange formalism, $N + 9$ equations of motion for the atomic coordinates \mathbf{s}_i and for the MD cell coordinates h_{kl} can be derived from Eq. (7.1) [201, 202].

Before writing the equations of motion we point out that their form will depend on the explicit form of K_{cell} . For the form of K_{cell} there are a number of proposals. One of the simplest is that by Parrinello and Rahman [202], which we will denote with K_{PR} here:

$$K_{\text{PR}} = \frac{w_{\text{PR}}}{2} \text{Tr}(\dot{h}^T \dot{h}). \quad (7.3)$$

In this case, the Euler-Lagrange formalism yields the equations of motion

$$\ddot{\mathbf{s}}_i = -\frac{1}{m_i} \sum_{j \neq i} \frac{\partial U(r_{ij})}{\partial r_{ij}} \frac{\mathbf{s}_i - \mathbf{s}_j}{r_{ij}} - g^{-1} \dot{g} \dot{\mathbf{s}}_i, \quad (7.4)$$

and

$$\ddot{h} = (\Pi - p_{\text{ext}}) \frac{\sigma}{w_{\text{PR}}}, \quad (7.5)$$

with

$$\Pi = \frac{1}{\Omega} \sum_{i=1}^N m_i \mathbf{v}_i \mathbf{v}_i^T - \frac{1}{\Omega} \sum_{i=1}^N \sum_{j>i} \frac{\partial U(\{r_{ij}\}, t)}{\partial r_{ij}} \frac{\mathbf{r}_{ij} \mathbf{r}_{ij}^T}{r_{ij}}. \quad (7.6)$$

Here, the definitions $g = h^T h$, $\mathbf{v}_i = h \dot{\mathbf{s}}_i$ and $\mathbf{r}_{ij} = \mathbf{r}_i - \mathbf{r}_j + h \mathbf{z}$ have been used and $\sigma = (\sigma_{\alpha\beta})$ with $\sigma_{\alpha\beta}$ calculated as $\sigma_{\alpha\beta} = \partial \Omega / \partial h_{\alpha\beta}$.

Improved choices of K_{cell} avoid the problem that K_{PR} does not fulfil the virial theorem [204, 203] and is not invariant with respect to the form of the MD supercell [203, 205]. The proposal by Cleveland reads [203]

$$K_C = \frac{w_C}{2} \text{Tr}(\dot{h} \sigma^T \sigma \dot{h}^T), \quad (7.7)$$

where σ is defined as in Eq. (7.5). With this term for K_{cell} inserted into the Lagrangian (Eq. (7.1)), the equations of motion for the relative atomic coordinates \mathbf{s}_i do not change with respect to Eq. (7.4), while those for the cell coordinates h become

$$\begin{aligned} \ddot{h} = & (\Pi - p_{\text{ext}}) \frac{h}{w_C \Omega} \\ & - \frac{2 \dot{\Omega} \dot{h}}{\Omega} + \text{Tr}(\dot{h} \sigma^T \sigma \dot{h}^T) \frac{h}{\Omega^2} + \frac{\dot{h} \sigma^T \dot{h}}{\Omega} + (\dot{h} \sigma^T \sigma \dot{h}^T - \sigma \dot{h}^T \dot{h} \sigma^T) \frac{h}{\Omega^2}. \end{aligned} \quad (7.8)$$

Here, the microscopic stress tensor Π is again calculated according to Eq. (7.6). (Note, in the last term of this equation a misprint in Eq. (18) of Ref. [203] has been corrected.)

In K_{PR} and K_{C} the parameters w_{PR} and w_{C} appear, and they play a role in the equations of motion for h that is analogous to that of the masses m_i in the equations of motion for the \mathbf{s}_i . Thus, while w_{PR} and w_{C} can be chosen as convenient for the calculation if only statistical averages over trajectories are determined, they must be chosen with care if dynamical properties are calculated. According to Andersen [201], these parameters should be adjusted so that the fluctuations of the MD supercell volume Ω take place on a time scale of $\sqrt[3]{\Omega}/c_M$, where c_M is the speed of sound in the material. For graphite and diamond, we have found $w_{\text{PR}} = M/25.5$ to fulfil this condition, where M is the total mass of all atoms in the MD supercell. For silicon, we use $w_{\text{PR}} = M/1.6$.

(ii) Ultrathin films. In this case the simulations are performed according to the geometry illustrated in Fig. 7.4. The MD cell is rigid, does not change its shape or volume in time, and defined by the constant primitive vectors $\mathbf{a} = (a, 0, 0)$, $\mathbf{b} = (0, b, 0)$ and $\mathbf{c} = (0, 0, c)$. Periodic boundary conditions in the lateral directions (defined by \mathbf{a} and \mathbf{b}) are used. Since the primitive vectors are rigid, this means that we do not allow expansion of the system in the lateral directions. This accounts for the inertial confinement which is produced by the rest of the film. In contrast, expansion of the system along the vertical directions \mathbf{c} and $-\mathbf{c}$ are, of course, allowed. This is achieved by setting a large value for the constant c , so that enough vacuum is present above and below the film. No assumptions are made regarding the external pressure. In view of the above discussion the second and the fourth terms of the Lagrangian (Eq. (7.1)) are dropped and the Lagrangian L_{film} for simulations on ultrathin films is given by

$$L = \sum_{i=1}^N \frac{m_i}{2} \dot{\mathbf{s}}_i^{\text{T}} h^{\text{T}} h \dot{\mathbf{s}}_i - U(\{r_{ij}\}, t). \quad (7.9)$$

Using the Euler-Lagrange equations we can again calculate the equations of motion for the atoms

$$\ddot{\mathbf{s}}_i = -\frac{1}{m_i} \sum_{j \neq i} \frac{\partial U(\{r_{ij}\}, t)}{\partial r_{ij}} \frac{\mathbf{s}_i - \mathbf{s}_j}{r_{ij}}. \quad (7.10)$$

These equations describe the motion of atoms in a MD supercell with periodical boundary conditions for the case that the cell size and shape does not change during the calculation. For the cell there are no equations of motion, since $\ddot{h} = 0$.

2.2 Potential energy surface: laser induced electron dynamics

The molecular dynamics techniques described above constitute a standard method to study structural properties of solids in thermodynamical equilibrium. In those cases, the potential energy surface $U(\{\mathbf{r}_{ij}\})$ is usually approximated by a model potential, like, for example, Lennard-Jones [206], Tersoff [207] or Stillinger-Weber [208], which consist of functions of the interatomic distances r_{ij} . For the description of laser induced structural changes, however, such model potentials are not useful, since they do not contain the electrons as degrees of freedom. Therefore, they do not allow any reasonable description of the excitation process. As mentioned at the beginning of this section, the laser pulse couples primarily with the electronic system. Hence, for the studies to be presented in this chapter, the many-body potential energy surface $U(\{\mathbf{r}_{ij}\}, t)$ must be derived from a microscopic electronic Hamiltonian.

We assume that the valence electrons of the covalent solid can be described by an effective single-particle Hamiltonian H_{eff} in a restricted Hilbert space spanned by M functions. H_{eff} depends, of course, on the electronic degrees of freedom, but also on the interatomic distances r_{ij} , since the properties of the electrons change if r_{ij} change. The effect of the rest of the core electrons and the internuclear repulsion is approximated by a repulsive potential $E_{rep}(\{\mathbf{r}_{ij}\})$. As effective Hamiltonian we use

$$H = \sum_{i\alpha} \epsilon_{i\alpha} n_{i\alpha} + \sum_{\substack{ij\alpha\beta \\ j \neq i}} V_{ij}^{\alpha\beta}(r_{ij}) c_{i\alpha}^+ c_{j\beta}. \quad (7.11)$$

Here, $\epsilon_{i\alpha}$ is the on-site energy of atom i and orbital α . $c_{i\alpha}^+$ and $c_{j\alpha}$ are the creation and annihilation operators, and $V_{ij}^{\alpha\beta}(r_{ij})$ the hopping integrals. For the description of carbon and silicon, the $2s$, $2p_x$, $2p_y$ and $2p_z$ orbitals are taken into account. For the radial part $R(r)$ of the hopping integrals and for E_{rep} we employ the forms proposed by Xu et al. [209]:

$$R(r) = \begin{cases} \left(\frac{r_0}{r}\right)^n \exp\left\{n\left[-\left(\frac{r}{r_c}\right)^{n_c} + \left(\frac{r_0}{r_c}\right)^{n_c}\right]\right\}, & r < r_1 \\ d_0 + d_1(r - r_1) + d_2(r - r_1)^2 + d_3(r - r_1)^3, & r \geq r_1 \end{cases} \quad (7.12)$$

$$E_{rep} = \sum_i f\left(\sum_j \phi(r_{ij})\right) \quad \text{with} \quad (7.13)$$

$$\phi(r) = \begin{cases} \phi_0 \left(\frac{d_0}{r}\right)^m \exp\left\{m\left[-\left(\frac{r}{d_c}\right)^{m_c} + \left(\frac{d_0}{d_c}\right)^{m_c}\right]\right\}, & r < d_1 \\ c_0 + c_1(r - d_1) + c_2(r - d_1)^2 + c_3(r - d_1)^3, & r \geq d_1 \end{cases} \quad (7.14)$$

Thus, for distances $r > r_1$ and $r > d_1$ respectively, the hopping integrals and $\phi(r)$ are replaced by polynomials that go to zero and are fitted smoothly to the

functions valid for $r < r_1$ and $r < d_1$. The repulsive potential E_{rep} is taken as a polynomial of the function $\phi(r)$. For all parameters in Eqs. (7.12)-(7.14) see Ref. [209].

The effective single-particle Hamiltonian $H_{\text{eff}}(\{\mathbf{r}_{ij}\})$ [Eq. (7.11)] yields M eigenvalues ϵ_m , which clearly depend on $\{\mathbf{r}_{ij}\}$.

The time-dependent potential energy surface $U(\{\mathbf{r}_{ij}\}, t)$ which governs the motion of the atoms is equal to the free energy of the electrons $F_{\text{el}}(\{\mathbf{r}_{ij}\}, t)$, and given by

$$U(\{\mathbf{r}_{ij}\}, t) = F_{\text{el}}(\{\mathbf{r}_{ij}\}, t) = \sum_m n(\epsilon_m, t) \epsilon_m + E_{\text{rep}}(\{\mathbf{r}_{ij}\}) - T_{\text{el}}(t) S_{\text{el}}(t), \quad (7.15)$$

where $n(\epsilon_m, t)$ are the occupations of the corresponding electronic levels ϵ_m . Due to the presence of the laser pulse, these occupations are time-dependent, as we show below. The first term of Eq. (7.15) represents the attractive contribution from the valence electrons. The third term contains the electronic temperature T_{el} and the electronic entropy S_{el} , which is given by

$$S_{\text{el}} = -k_B \sum_m [n(\epsilon_m, t) \log(n(\epsilon_m, t)) + (1 - n(\epsilon_m, t)) \log(1 - n(\epsilon_m, t))]. \quad (7.16)$$

Note that the functional dependence of $U(\{\mathbf{r}_{ij}\}, t)$ on the interatomic distances $\{\mathbf{r}_{ij}\}$ is strongly dominated by the electronic occupations $n(\epsilon_m, t)$ present in the first and third terms of Eq. (7.15). If the electronic occupations undergo strong changes, then the potential energy landscape $U(\{\mathbf{r}_{ij}\}, t)$ will change significantly.

In view of the above discussion one can understand the mechanisms for laser induced structural changes by using a simple physical picture sketched in Fig. 7.5. Before laser heating the solid is in thermodynamical equilibrium at a low initial temperature ($T_i \leq 300K$). This means that electrons fill mainly the states below the Fermi level. The resulting ground state potential landscape $U_i(\{\mathbf{r}_{ij}\})$ shows minima at the crystal lattice sites. Atoms are sitting on these sites and therefore no forces act on them. However, the situation changes dramatically when the solid becomes heated by a laser pulse. For moderate and high fluences the laser creates a considerable amount of electron-hole pairs, as illustrated in Fig. 7.5. This means that the electronic occupations $n(\epsilon_m, t)$ change. Consequently, the functional form of $U(\{\mathbf{r}_{ij}\})$ undergoes quantitative and qualitative changes, which result in the disappearance or shifting of the minima. Since these modifications occur on a time scale which is much shorter than the reaction time of the lattice, the atoms remain in their positions, most of them no longer minima of the new potential landscape. Therefore, forces act now on the atoms, which start to move. This is the way laser induced structural changes take place.

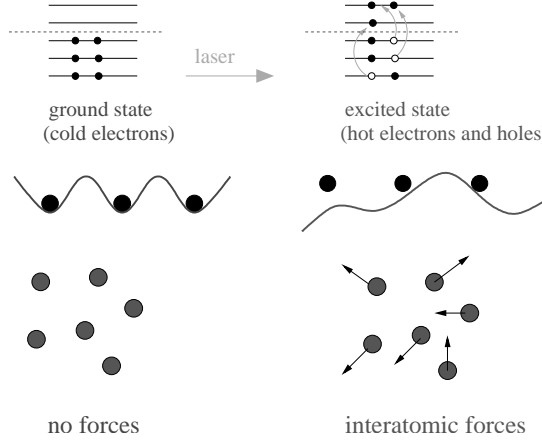


Figure 7.5: Illustration of the microscopic physical picture derived from Eq. (7.15). a) Situation before the action of the laser pulse: the solid is in thermodynamic equilibrium. For low temperatures electrons fill the states up to the Fermi level. The atoms are at the equilibrium positions of the ground state potential energy surface. b) The laser pulse changes the electronic occupations. This leads to rapid changes in the potential energy landscape. As a consequence, the lattice becomes unstable and forces on the atoms appear, driving a structural change.

Fig. 7.5 does not show how the electron occupations change in time. This is a fundamental point, which must be taken carefully into account by any theory aimed at the description of laser induced structural effects. In order to obtain an equation for the rate of change of the electron occupations $n(\epsilon_m, t)$ we consider the equation of motion for the density matrix $\hat{\rho}$, which reads

$$\dot{\hat{\rho}} = -\frac{i}{\hbar} [H_{TB} + V_{laser}, \hat{\rho}] + \left. \frac{\partial \hat{\rho}}{\partial t} \right|_{coll}. \quad (7.17)$$

The first term refers to the coherent motion of the electrons, which is driven by the laser field and which involves optical transitions between the energy levels of the Hamiltonian H_{TB} . Since the tight-binding Hamiltonian is a single-particle one, it does not describe interactions between the excited electrons, which are essential for the thermalization processes. Thus, we treat them by including a second, dissipative term in Eq. (7.17).

Eq. (7.17) represents a system of coupled differential equations for the diagonal and nondiagonal elements of the density matrix. However, since the electron-hole plasma created by the laser undergoes rapid dephasing, the relevant equations of motion will be those describing the diagonal elements. There-

fore, neglecting the contribution of the nondiagonal elements one obtains [210]

$$\frac{dn(\epsilon_m, t)}{dt} = \int_{-\infty}^{\infty} d\omega g(\omega, t - \tau) \left\{ [n(\epsilon_m - \hbar\omega, t - \tau) + n(\epsilon_m + \hbar\omega, t - \tau) - 2n(\epsilon_m, t - \tau)] \right\} - \frac{n(\epsilon_m, t) - n^0(\epsilon_m, T_{el})}{\tau_1}. \quad (7.18)$$

Here, the first (integral) term describes the laser excitation and creation of a nonequilibrium electron distribution. $g(\omega, t)$ is the intensity function of the laser pulse, which describes the intensity as a function of frequency and time as a product of the time envelope and its Fourier transform. Thus, the electronic distribution is at each time step folded with the current intensity function $g(\omega, t)$. This means that at each time step, the occupation of an energy level ϵ_m changes in proportion to the occupation difference with respect to levels at $\epsilon_m - \hbar\omega$ and at $\epsilon_m + \hbar\omega$. In Eq. (7.18), the optical matrix elements are assumed to be equal to unity, so that the band structure plays the main role in the absorption process. This simplification makes sense, as the calculation of optical matrix elements is at the same time tedious and known to be rather inaccurate in the TB approximation. Eq. (7.18) can be straightforwardly generalized to include the dipole matrix elements. The second term of Eq. (7.18) describes the electronic thermalization resulting from electron-electron collisions through a relaxation time τ_1 . Thus, with a time constant τ_1 , the distribution $n(\epsilon_m, t)$ approaches a Fermi-Dirac distribution $n^0(\epsilon_m, T_e)$, which is given by

$$n^0(\epsilon_m, T_e) = \frac{1}{\exp\{\beta(\epsilon_m - \mu) + 1\}}, \quad \text{with } \beta = \frac{1}{k_B T_e}. \quad (7.19)$$

Here, T_e is the electron temperature, and μ is the chemical potential. This simple approach works very well because for dense electron-hole plasmas in covalent solids extremely low relaxation times τ_1 have been found. Chemla and coworkers have reported a carrier thermalization faster than 10 fs in GaAs [211]. Thus, we use $\tau_1 = 10$ fs throughout this chapter. Note, for such a short thermalization time the exact electronic dynamics leading to electronic equilibrium do not play a significant role for the structural changes we are studying here.

The electronic temperature T_e and the chemical potential μ , which appear in the Fermi-Dirac distribution and which are not determined by Eq. (7.18), need to be fixed by an additional principle. We will demand that the nonequilibrium distribution $n(\epsilon_m, t)$ approaches the Fermi-Dirac distribution while conserving the total energy of the system. Energy loss mechanisms, which are of course already present as soon as some laser energy has been absorbed, will be treated in the following section in a way that does not interfere with this principle of

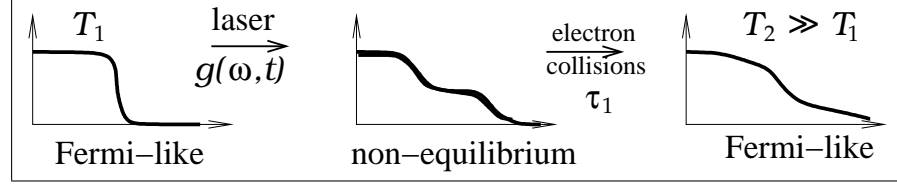


Figure 7.6: Illustration of the electron excitation and thermalization processes described by Eq. (7.18). The temperature T_2 reached after thermalization is much higher than the initial temperature T_1 , since the electron system has absorbed energy from the laser pulse.

energy-conserving equilibration. The total energy at time t is required to be

$$E_{\text{tot}}(t) = U(\{r_{ij}(t)\}, t) + E_{\text{kin}}(t) \stackrel{!}{=} E_{\text{tot}}(t=0) + E_{\text{abs}}(t) - E_{\text{loss}}(t), \quad (7.20)$$

where $E_{\text{kin}}(t)$ is the kinetic energy of the ions, and $E_{\text{abs}}(t)$ is the energy that has been absorbed from the laser pulse up to the time t . A further, obvious demand which is necessary to determine T_e and μ is that the number of electrons N_e stays constant over the entire calculation:

$$N_e(t) = \sum_m n(\epsilon_m, t) \stackrel{!}{=} N_e^0. \quad (7.21)$$

Thus, by enforcing conservation of energy during the electron thermalization we make sure that we get physically meaningful results. In Fig. 7.6 the processes of excitation and thermalization are illustrated.

With this approach the effect of a laser-induced electronic nonequilibrium on the structural response can be studied. This theory for the time dependence of the occupation numbers would be too simple if electron dynamics during the first few femtoseconds after laser excitation were in the centre of our study. However, the main focus of this work are laser-induced structural changes on a time scale of a few picoseconds. These are not expected to be very sensible to fine details of the nonequilibrium distribution created by the laser pulse. Thus, Eq. (7.18) is used for the study of the dependence of structural relaxation on duration, frequency and intensity of the exciting pulses.

2.2.1 Summary of the numerical approach. Our theoretical description of laser induced structural changes requires to solve in a parallel way the classical equations of motion for the nuclear degrees of freedom (and also of the lattice vectors, in the case of simulations at constant pressure) and the equations of motion for the electronic occupations [Eq. (7.18)]. The equations of motion are, of course, coupled. Changes in the occupations lead to changes in the potential energy surface. These lead to changes in the atomic coordinates (due to the presence of forces on the atoms) which cause changes in the

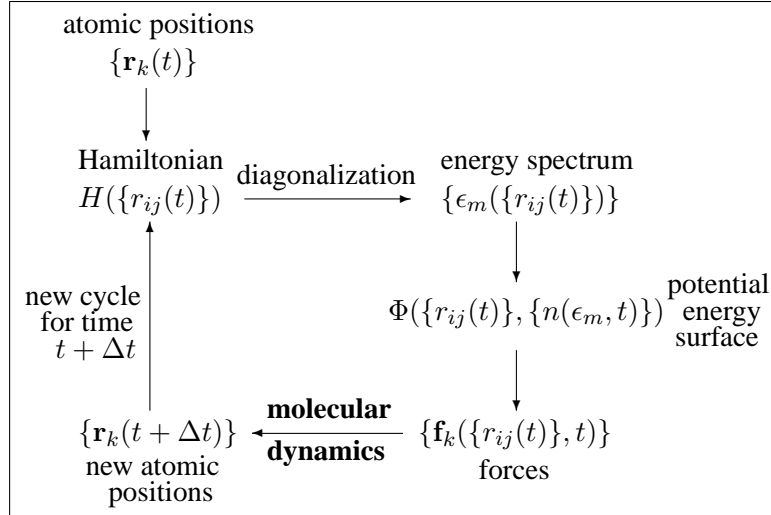


Figure 7.7: Molecular dynamics scheme for the determination of changes of the atomic structure in response to electronic excitation. An explicitly time dependent potential energy surface (PES) is obtained on the basis of an electronic Hamiltonian and with the help of a time dependent nonequilibrium electronic occupation. This PES yields forces for the MD. Then these are used to work out the relaxation of the atomic structure.

eigenvalue-spectrum of the Hamiltonian H_{TB} (due to changes of the hopping matrix elements).

In Fig. 7.7, our calculation procedure is summarized. It is important to point out, that for each time-step of our simulations we have to diagonalize H_{TB} and also solve Eqs. (7.20) and (7.21) to determine the instantaneous electron temperature and chemical potential.

A further technical point which is important to mention is that the calculation of the forces from the expression (7.15) for the potential energy surface $U(\{\mathbf{r}_{ij}\}, t)$ does not involve the gradients of the electron occupations. It has been shown [212, 213] that the correct lattice dynamics is obtained by taking only the gradients of the eigenvalues of H_{TB} and of the repulsive potential in Eq. (7.15) without further terms involving derivatives of the occupation numbers $n(\epsilon_m, t)$. This is because the terms arising from the gradients of $n(\epsilon_m, t)$ in the first and third terms of (7.15) approximately cancel out (except for negligible corrections).

2.2.2 Pair correlation function. For the characterization of the structural changes during a solid to liquid phase transition, a meaningful quantity is needed. The pair correlation function (or radial distribution function) $g(r)$ is the density of other particles around a given particle. This function has a sharply peaked structure in a perfect crystal, while in a liquid, it shows structure only

for small r . It is normalized so that at large r , $g(r) = 1$. Thus, it is given by [214, 215]

$$g(r) = \frac{\langle \Delta N(r) \rangle}{n_a 4\pi r^2 \Delta r} \quad (7.22)$$

where $\Delta N(r)$ is the number of atoms situated at a distance between r and $r + \Delta r$ around a given particle, and $n_a = N/\Omega$ is the atomic density of the material. The denominator of Eq. (7.22) corresponds to the average number of particles in the spherical shell of radius r and thickness Δr . The average $\langle \dots \rangle$ is performed over all atoms in the material sample.

The pair correlation function will show a strong peak at the nearest neighbour distance r_{nn} . For higher distances, peaks of decreasing amplitude will indicate more distant neighbours around a particle.

3. Ultrafast nonequilibrium graphitization of diamond

A most interesting process observed in diamond between damage and ablation thresholds is shown in Figs. 7.9 and 7.10.¹ It is an ultrafast nonequilibrium graphitization of diamond. In Figs. 7.9 and 7.10 we show detailed snapshots of a graphitization trajectory. The laser pulse of $\tau = 20$ fs duration had an energy of $E_0 = 1.0$ eV/atom which is very close to the damage threshold of diamond. In Fig. 7.8 the time evolution of the corresponding MD supercell volume is shown. The material was initially thermalized to a temperature of $T = 300$ K. Upon incidence of the ultrashort laser pulse at $t = 0$ fs, the material expands sharply due to the weakening of the bonds by the laser excitation. The cohesion of the lattice is still strong enough so that the expansion peaks at $t = 20$ fs, and the material contracts again. This ultrafast “breathing” of the material occurs once more, with an expansion maximum at $t = 107$ fs. The third expansion of the lattice turns out to be irreversible: The expansion and contraction cycles have caused small rearrangements of the atoms which now lead to bond breaking between several of the diamond planes, and the armchair-shaped hexagons of the diamond lattice begin to straighten out. The graphitization starts at the upper left side of the MD supercell and propagates into the remaining three dimensionally bonded material during the following 80 to 100 fs. At $t = 240$ fs, perfect graphite planes have formed. Nevertheless, these planes are still strongly vibrationally excited and relaxation of the high electronic temperature must take place before a permanent final graphite state is produced.

¹Fig. 7.9 as well as Figs. 7.10, 7.15, 7.17, 7.18, 7.21, 7.23 and 7.24 were produced with the help of BALSAC (version 2.12, (C) Copyright K. Hermann 1991-9). The BALSAC software was developed by K. Hermann, Fritz-Haber-Institut Berlin (Germany).

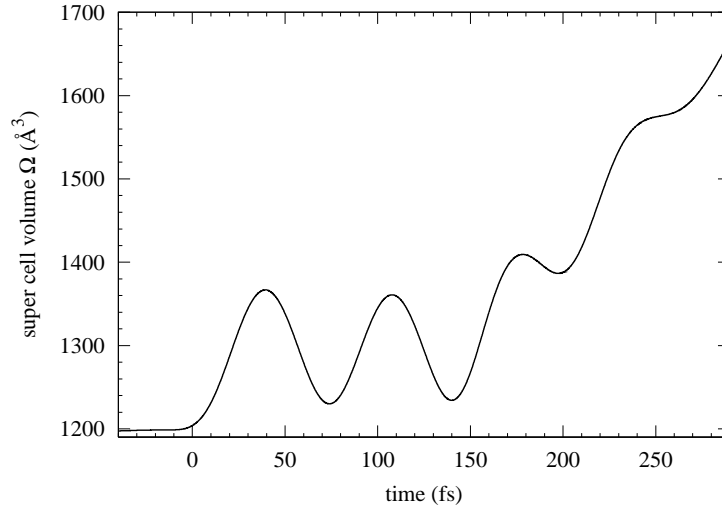


Figure 7.8: Time evolution of the MD super cell volume of a (100) diamond sample during ultrafast graphitization. Time is measured with respect to the maximum of the laser pulse with a duration of $\tau = 20$ fs. The pulse triggers two rapid expansions of the material with subsequent contractions before the graphitization sets in at app. $t = 200$ fs. At this time, strong expansion of the material sets in.

This result, shown in Figs. 7.9 and 7.10 for a (100) diamond MD supercell at constant pressure, has been observed for a large range of laser pulse durations and intensities; in fact, for the entire pulse duration and intensity region between the damage and the ablation thresholds, an ultrafast graphitization is the first relaxation process. The theoretical observation of this laser-induced graphitization has also been confirmed by calculations for a film geometry.

The MD calculation for the bulk material at constant pressure was performed at $P = 10^5$ Pa. The trajectories determined by this method correspond to an isobaric-isoenthalpic ensemble. This means that the entire MD supercell is subjected to an isotropic constant pressure. Note that our volume expansions upon graphitization relate to the considered subregion due to our use of a MD supercell with periodic boundary conditions. While the electronic transition $sp^3 \rightarrow sp^2$ behind the graphitization occurs very fast (in less than 50 fs), the time scale for the following volume and shape changes is characterized by a velocity of typically $v_{cp} \approx 0.03$ Å/fs, which may be compared with the velocity of sound in diamond, $c_D = 0.18$ Å/fs. Thus, although the theoretically observed graphitization occurs on a femtosecond time scale, it involves lattice deformations at a velocity well below the theoretical upper limit defined by the sound velocity.

In Fig. 7.11 we show the densities of states corresponding to the graphitization process of Figs. 7.9 and 7.10. In addition to the total DOS, σ and π

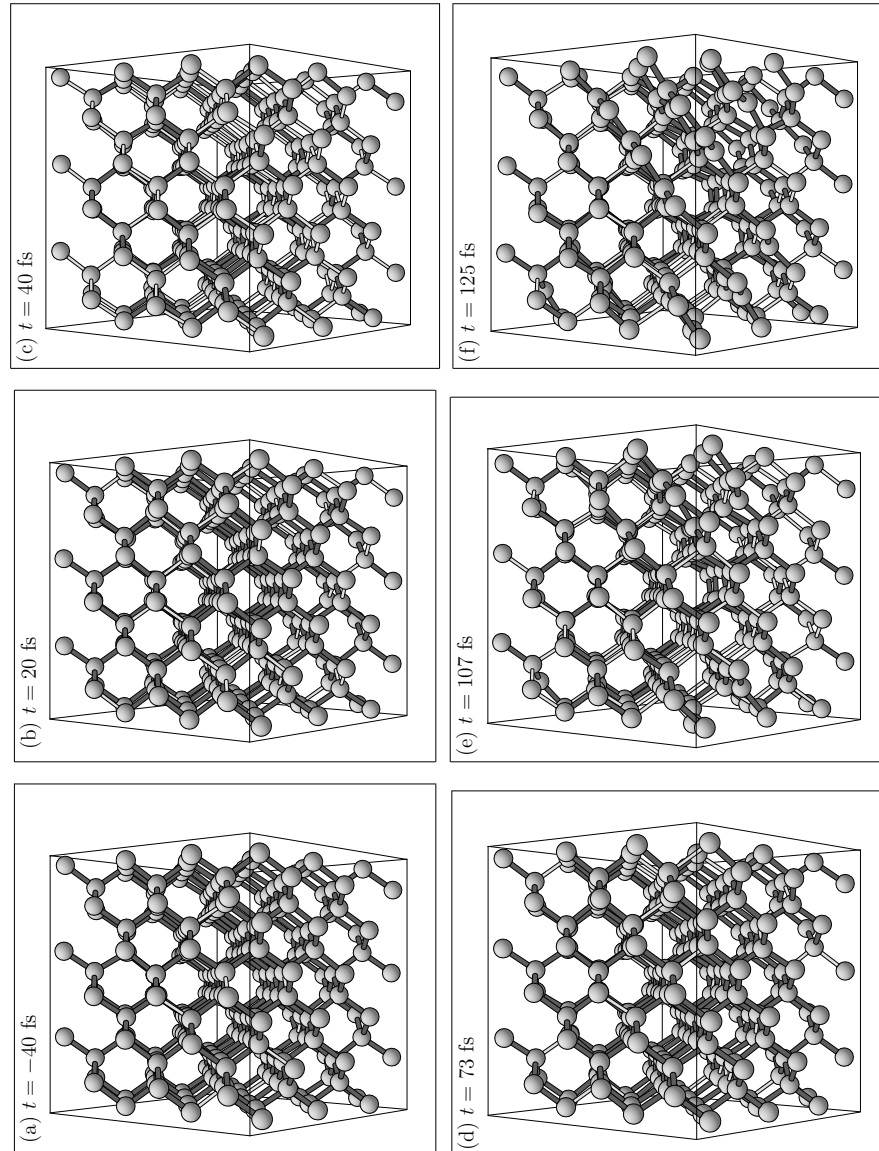


Figure 7.9: Ultrafast graphitization of a (100) diamond crystal (initial stage). The energy $E_0 = 1.0$ eV/atom was absorbed from the laser pulse of $\tau = 20$ fs duration. The MD supercell contains $N = 216$ atoms. Bonds up to a length of $l = 1.6$ Å are drawn in dark grey, weaker bonds of $1.6 \text{ Å} < l < 2.0$ Å in light grey. For a description of the transformation see the text.

contributions are shown. The DOS should be compared to the DOS of ideal diamond and graphite shown in Fig. 7.12 (a) and (b).

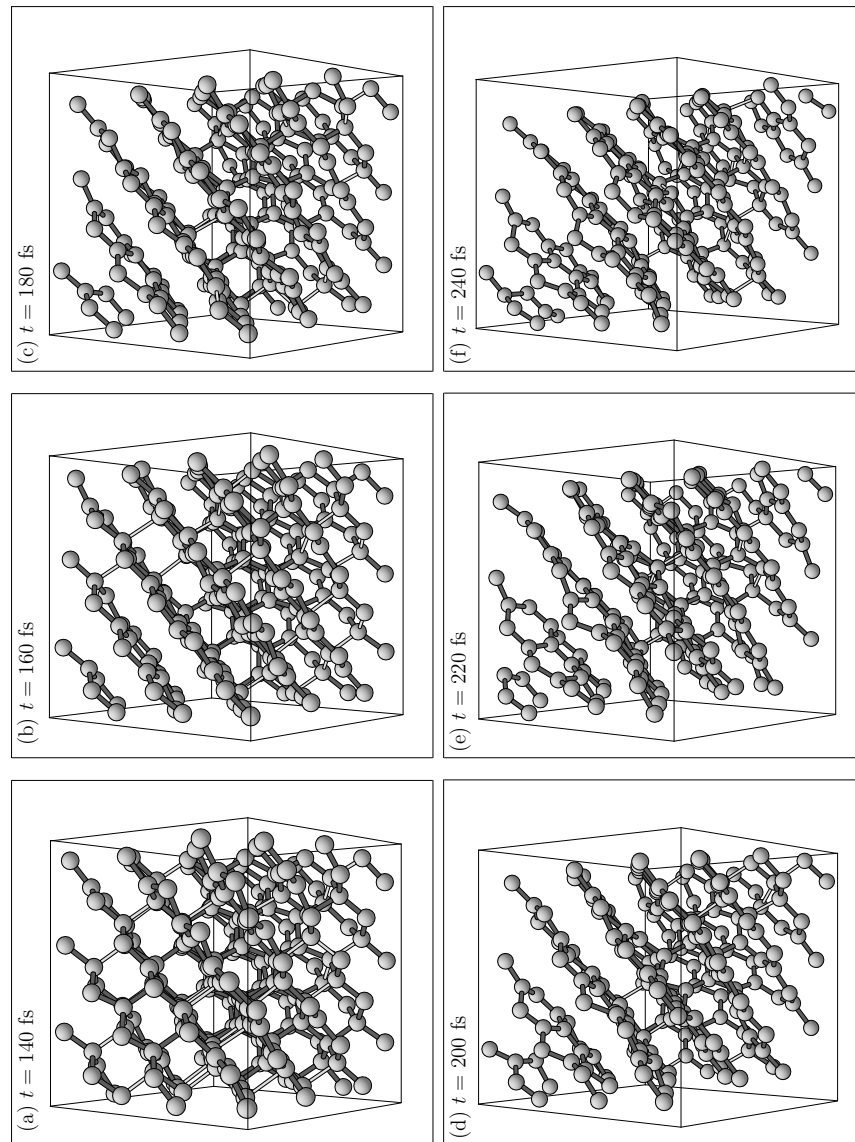


Figure 7.10: Ultrafast graphitization of a (100) diamond crystal (later stage). The energy $E_0 = 1.0$ eV/atom was absorbed from the laser pulse of $\tau = 20$ fs duration. The MD supercell contains $N = 216$ atoms. Bonds up to a length of $l = 1.6$ Å are drawn in dark grey, weaker bonds of $1.6 \text{ Å} < l < 2.0$ Å in light grey. For a description of the transformation see the text.

At a time $t = 10$ fs (see Fig. 7.11 (a)), measured from the maximum of the laser pulse of $\tau = 20$ fs duration, the DOS is still that of intact diamond

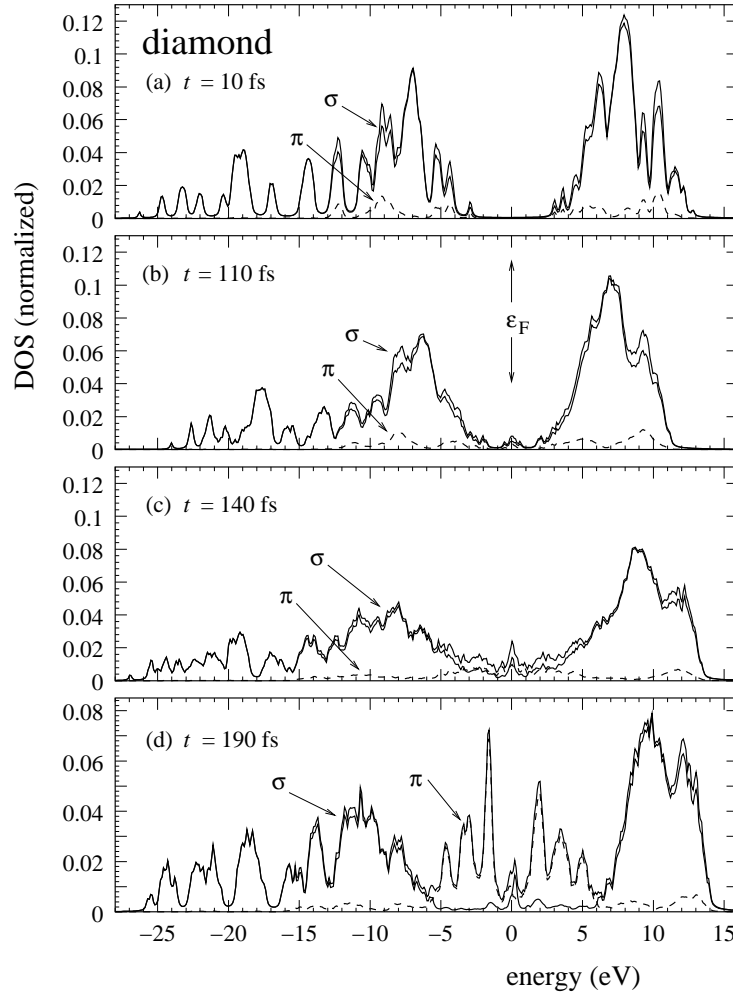


Figure 7.11: Densities of states during a nonequilibrium graphitization of diamond. The time is given with respect to the peak of a laser pulse of $\tau = 20$ fs duration. The densities of states correspond to the structures in Figs. 7.9 and 7.10. The π contribution to the DOS is indicated by a dashed line. Note, the ordinate scale of (d) has been changed with respect to (a)-(c). For a detailed description of the changes to the DOS see the text.

with a very small π contribution and a gap of $E_g = 5.5$ eV. At $t = 120$ fs (see Fig. 7.11 (b)), the structures of diamond DOS are broadening, and we see the emergence of a small number of states in the gap. At $t = 140$ fs (see Fig. 7.11 (c)), the structures of the diamond DOS have broadened even further, and close to the Fermi level, the density is increasing. This increase is to a large part due to π states. At $t = 190$ fs, (see Fig. 7.11 (d)) the features of the graphite DOS have developed. The π states now contribute strongly to the DOS, forming the structures on both sides of the Fermi level. These structures

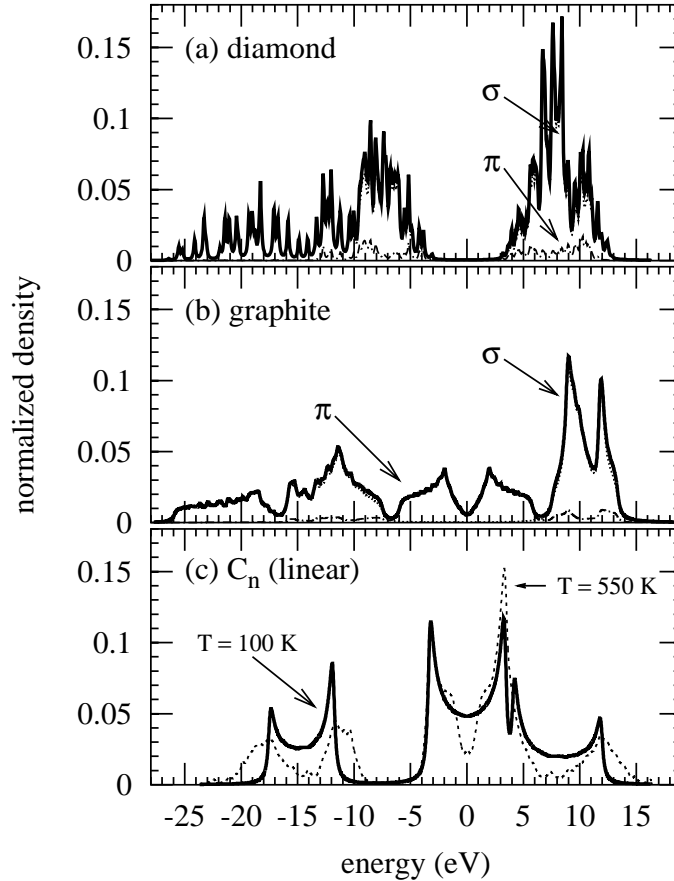


Figure 7.12: Densities of states of (a) diamond, (b) graphite, and (c) linear carbon chains. The DOS of diamond and graphite are computed at $T = 0$ K, while the DOS of C_n chains is given at $T = 100$ K (solid line) and $T = 550$ K (dashed line). For diamond and graphite, the solid lines indicate the total DOS, while σ and π contributions to the DOS are indicated by dotted and dash-dotted lines, respectively. For all graphs, the Fermi level ϵ_F determines the zero of the energy scale. (a) In the case of diamond, the material is characterized by the very large band gap of $E_g = 5.5$ eV. The DOS is dominated by the σ bonds of the sp^3 hybridized valence orbitals. The contribution of π electrons to the DOS is almost negligible. (b) In the case of graphite, the structures on both sides of the Fermi level ϵ_F are almost exclusively formed by the π bonds, while the remainder of the DOS reflects the σ bonds of the sp^2 hybridized orbitals. The fact that the DOS is slightly above zero at the Fermi level is an artifact caused by the broadening of the energy levels with Lorentzians of a width $\gamma = 0.1$ eV. (c) For the linear carbon chains, the higher temperature leads to a significant broadening of the structures. As in graphite, the structures on both sides of the Fermi level ϵ_F are determined by π bonding, while the rest of the DOS reflects σ bonds. As in a linear chain only two of the valence orbitals take part in the sp hybridization, the weight of the π contributions to the DOS is increased compared to graphite.

show relatively sharp spikes when compared to the DOS of graphite at $T = 0$ K. These can be attributed to the strong vibrational excitation of the graphite that has been newly formed from diamond.

4. Ablation mechanisms in graphite

In this section we present results for damage and ablation thresholds of graphite, and we analyze in detail the structural changes occurring above these two distinct thresholds. The thresholds have been calculated for bulk materials at a constant pressure of $P = 10^5$ Pa. Under ablation threshold we understand the deposited energy that is necessary to completely destroy the cohesion of the graphite planes and vaporize the material within 2 ps after the peak of the laser pulse. Even at laser intensities somewhat below the threshold determined in this way, the deposited energy may be sufficient to melt and vaporize the material on a time scale of tens or hundreds of picoseconds which is not accessible to our calculations. Thus, the thresholds for ultrafast ablation shown here can be considered as upper limits for the ablation thresholds found in the experiment by *post mortem* analysis of the sample. The damage threshold is determined by the energy density that causes, again within 2 ps after the pulse, significant structural changes without completely destroying the cohesion of the material.

In Fig. 7.13, we show the ablation threshold for graphite as a function of pulse duration. It was calculated using a MD cell containing $N = 64$ atoms. As in the case of diamond the ablation is defined as an evaporation of the material. Below the ablation threshold interesting structural changes occur and Fig. 7.13 shows a damage threshold that is approximately 1 eV lower in energy than the ablation threshold. Calculation with a much higher number of atoms ($N = 576$) in a film geometry confirmed that in fact a second ablation threshold below the one presented in Fig. 7.13 can be distinguished. It includes a strong vibrational excitation of the graphite planes. These remain intact, but they collide because of the strong oscillation of the atoms perpendicular to the planes and then, ablation of entire planes can occur as a consequence of the momentum transferred in these collisions. This process will be described in detail below.

Both thresholds shown in Fig. 7.13 increase very slightly with pulse duration, but this effect is not very pronounced.

The examination of a graphite film which had absorbed a moderate energy density has produced a surprising result: There is an ablation mechanism which does not lead to a destruction of the graphite planes. The principle of this mechanism is illustrated in Fig. 7.14. The graphite planes are separated in thermal equilibrium by a very large distance of $d = 3.4 \text{ \AA}$ and consequently their interaction is given by a very weak van-der-Waals energy of $E \approx 20 \text{ meV}$. Meanwhile, a photoinduced electron-hole plasma can lead to a very strong vibrational excitation of the graphite layers, and at the turning point of their oscillations the atoms of two different layers can come as close as $d \approx 2 \text{ \AA}$. At this distance, the interaction becomes already quite strong and is on the order of $E \approx 1 \text{ eV}$. In other words, the laser-induced strong vibrations can lead to

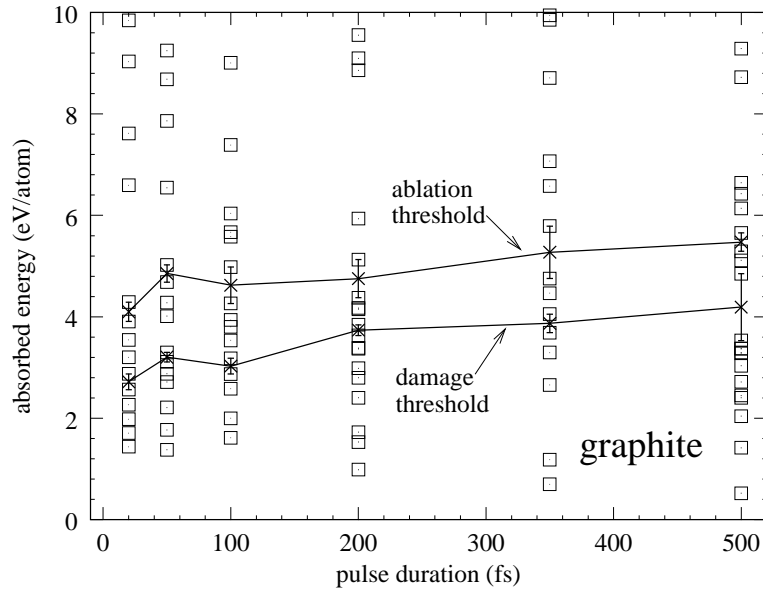


Figure 7.13: Ablation threshold of graphite as a function of laser pulse duration. Each result (\square) in the figure corresponds to a trajectory calculated for a $N = 64$ atom MD supercell.

collisions of the planes in which momentum is transferred. Thus, a plane on the surface of a graphite sample which usually has zero total momentum can gain enough momentum to leave the surface.

In Fig. 7.15 we present snapshots of the dynamics of graphite for a $\tau = 20$ fs laser pulse with an absorbed energy of $E_0 = 2.4$ eV/atom. The number of atoms is $N = 576$, and they are in a film geometry, *i. e.* the material has periodical boundary conditions in the horizontal directions, while in the vertical direction it borders on large slabs of vacuum. This film was thermalized to a temperature of $T = 300$ K before the action of the laser pulse. The trajectory of Fig. 7.15 shows the very interesting new ablation mechanism. At a deposited energy density that is far below the ablation threshold we find the ablation of entire graphite planes by the mechanism explained above: The laser pulse leads to a strong vibrational excitation of the graphite layers, with a significant movement of the atoms perpendicular to the graphite planes. This excitation is already strong at $t = 80$ fs after the laser pulse maximum, but for the topmost plane it reaches a maximum at $t = 160$ fs (see Fig. 7.15). At that time the distance between the graphite planes has narrowed to approximately $d = 1.8$ Å, and the first and second planes strongly interact. We can speak of a collision of the two topmost graphite planes, which then leads to a momentum transfer. Consequently, the surface plane that had up to that time zero total momentum

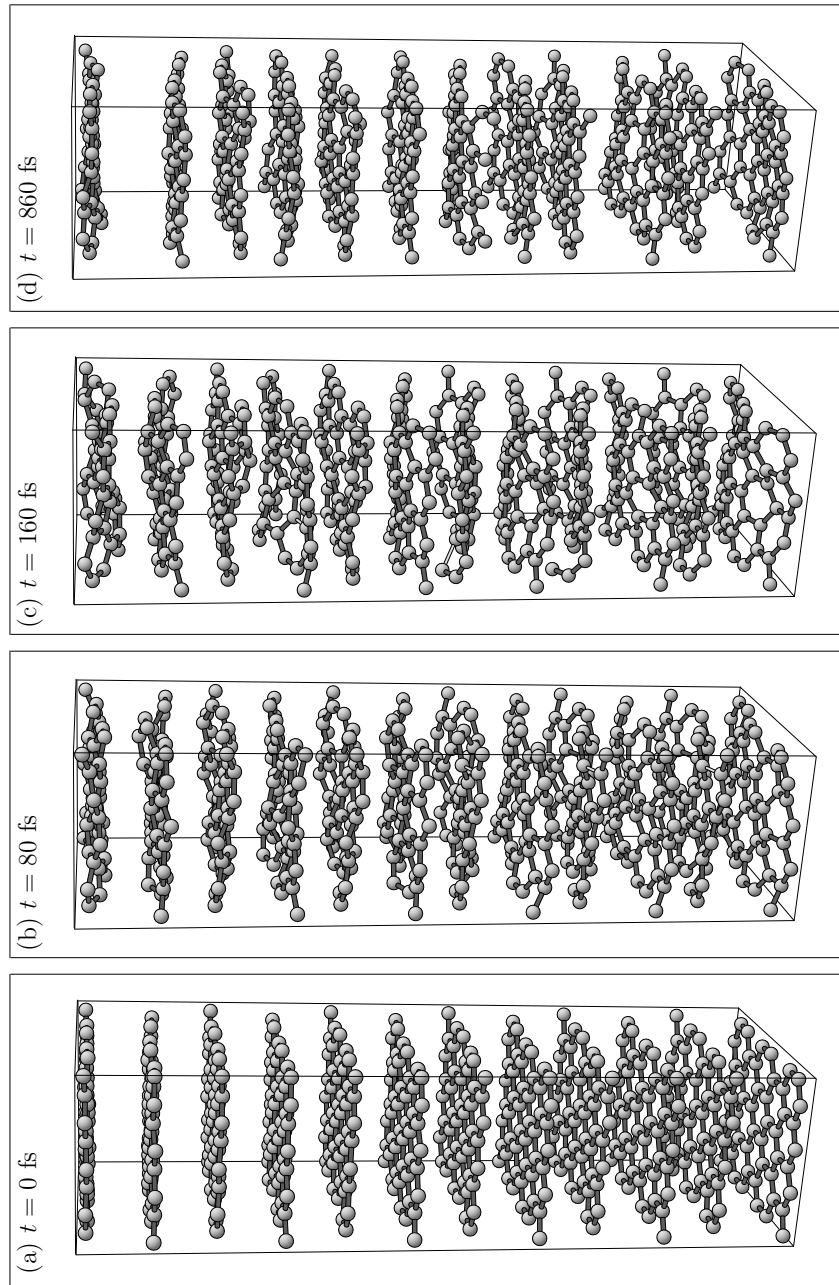


Figure 7.15: Ablation of graphite at an absorbed energy of $E_0 = 2.4$ eV/atom. The pulse duration was $\tau = 20$ fs. This energy density is below the threshold for the destruction of graphite planes. Thus, the laser energy is transferred into a very strong vibration of the graphite planes. At $t = 160$ fs, this vibration leads to a collision of the planes, during which momentum is transferred. As a consequence, the planes at the top and at the bottom are removed from the surface of the film.

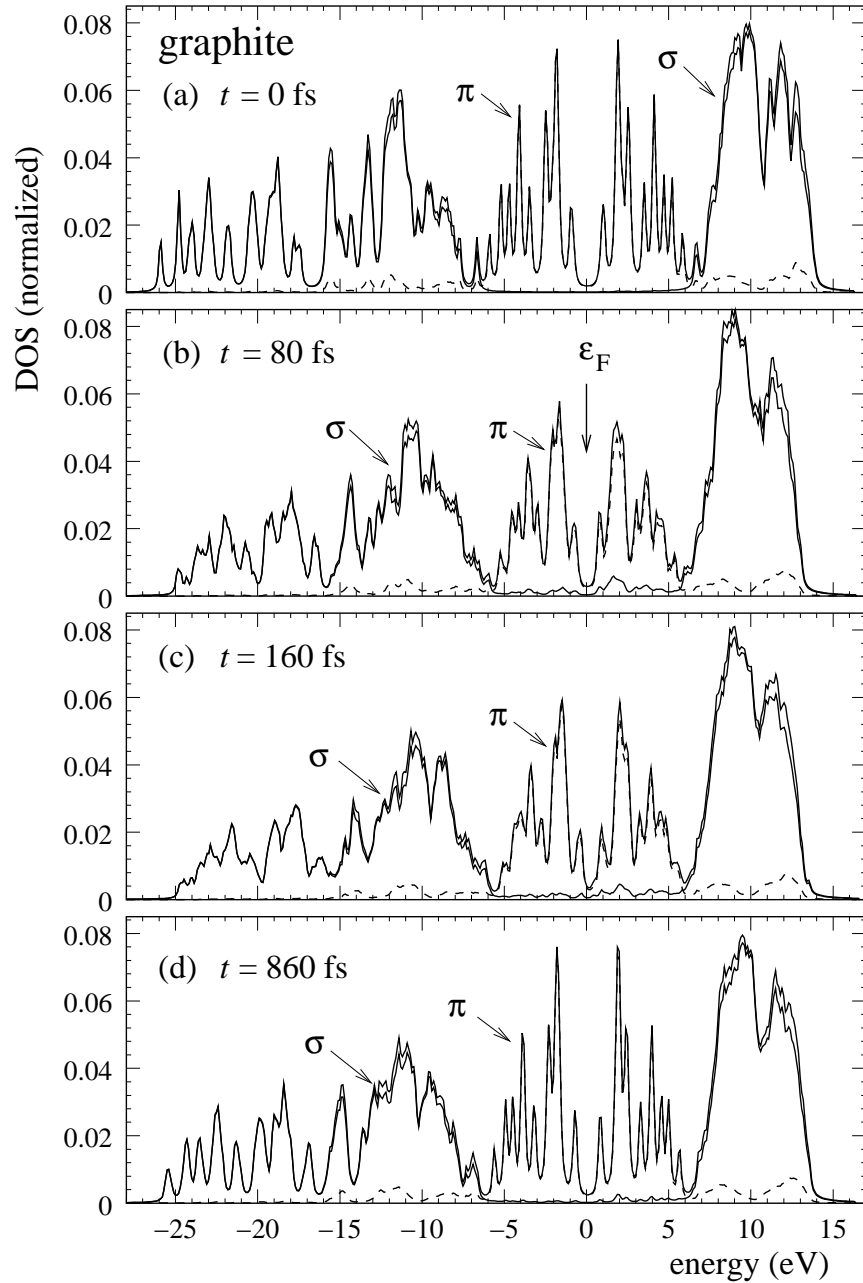


Figure 7.16: Densities of states for the ablation of graphite at an absorbed energy of $E_0 = 2.4$ eV/atom. This figure corresponds to the trajectory of Fig. 7.15. The π contribution to the DOS is indicated by a dashed line. Due to the strong vibrational excitation of the graphite planes at $t = 80$ fs and $t = 160$ fs the π contribution to the DOS is slightly diminished and the corresponding structures in the DOS are broadened. At $t = 860$ fs the DOS is recovering its original shape, corresponding to the falling amplitude of the vibrations in Fig. 7.15 (d).

5. Nonequilibrium melting and ablation of carbon

The processes leading to a melting of graphite are of high fundamental interest. While thermal melting has been studied already [183], the nonequilibrium melting discussed in this section has not been analyzed theoretically before. This study is important for a great number of experiments where nonequilibrium conditions are induced in carbon materials.

In Fig. 7.17 and Fig. 7.18 we show snapshots of a long trajectory of a graphite film in which melting and subsequent evaporation can be observed. The film consists of $N = 576$ atoms. The dynamics shown are for a $\tau = 20$ fs laser pulse with an absorbed energy of $E_0 = 4.0$ eV/atom. This energy density is high enough to break the bonds of the graphite planes. After $t = 40$ fs, we see that especially in the lower part of the film, bonds are formed between the graphite planes. Note, the initial graphite film was thermalized to $T = 300$ K, so that at the time the laser pulse hits the material all atoms are in an individual state of motion. This determines the initial conditions for the amplified oscillations due to the presence of the electron-hole-plasma. Thus, it is not surprising that on a very short time scale there are differences in the motion of different graphite planes. At $t = 80$ fs, we can see already the first carbon monomer being evaporated from the material, confirming that the graphite planes have been excited above their fragmentation threshold. In the following snapshot at $t = 140$ fs, four further monomers are leaving the two surfaces of the film and the graphite planes have been dissolved completely.

In Fig. 7.18, the further time development of the excited graphite sample of Fig. 7.17 is shown. In the snapshots presented here, a strong volume expansion is observed, *e. g.* from 5480 \AA^3 at $t = 220$ fs to 6040 \AA^3 at $t = 320$ fs. This expansion is reflected in Fig. 7.18 in the decreasing width of the column of the material rather than in an increasing z extension of the column which would have made for an awkward representation in the figures. In all graphs of Fig. 7.18, four monomers that had already moved far away from the surface were omitted. Fig. 7.18 now shows the advancing ablation process. Further carbon monomers are ejected from the material, and between $\Delta t = 420$ fs and $\Delta t = 920$ fs we can observe how the expansion of the material takes place especially rapidly in the two surface regions of the film, leading to low densities and the formation of short carbon chains which then start to leave the sample.

In Fig. 7.19 we show the densities of state that correspond to Fig. 7.17. At $t = 80$ fs (see Fig. 7.19 (b)) the features of the graphite DOS have already significantly broadened, and at the Fermi level the DOS has increased. In Fig. 7.19 (c) for $t = 160$ fs, the DOS has become metallic-like. The sharp spike close to the Fermi level corresponds to features of the DOS of the linear chain (see Fig. 7.12 (c)). These features have developed further in Fig. 7.19 (d)) for $t = 860$ fs.

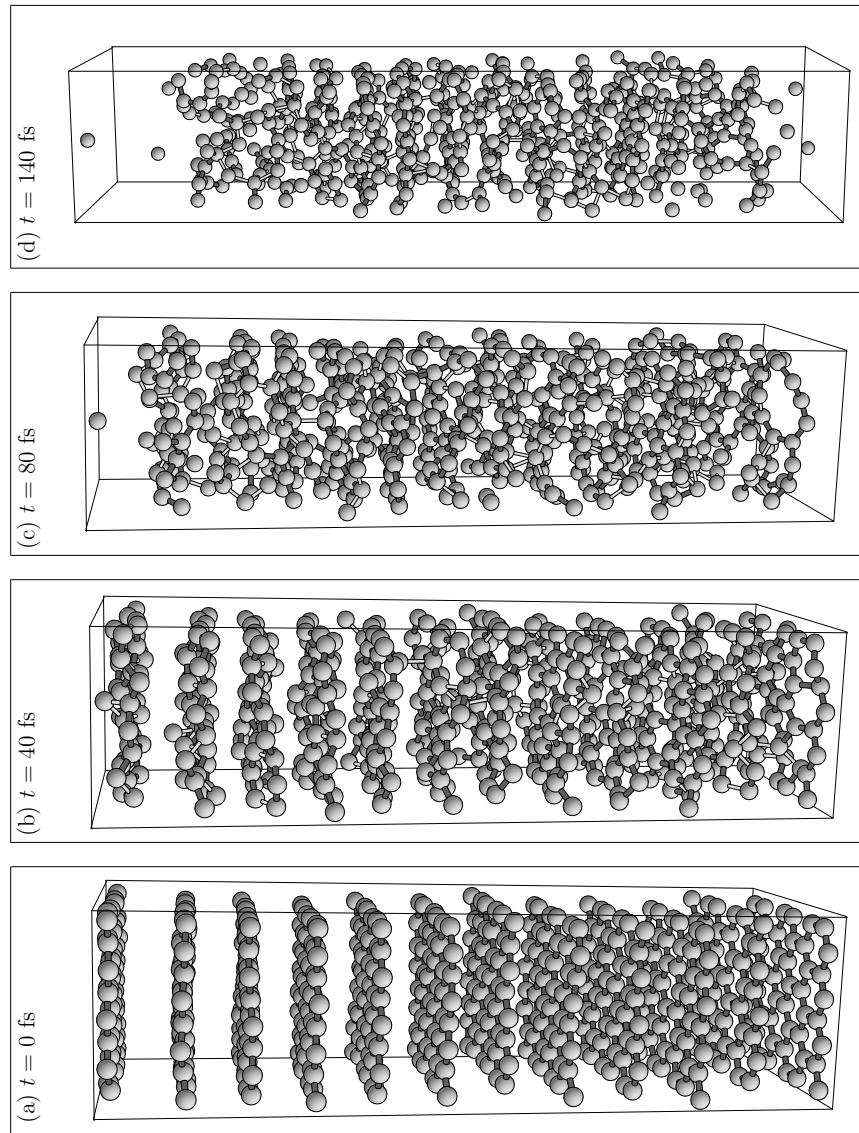


Figure 7.17: Ablation of a graphite film at an absorbed energy of $E_0 = 4.0$ eV/atom. The laser pulse duration was $\tau = 20$ fs. This figure shows the early stages of the ablation process (for the later stages see Fig. 7.18). The graphite planes vibrate strongly (b) and are destroyed (c) in response to the electron-hole plasma. At $t = 140$ fs the material is in violent motion (d), and carbon monomers are emitted.

In Fig. 7.20 we show the pair correlation functions $g(r)$ during the melting of a graphite film. The pair correlation functions of Fig. 7.20 correspond to

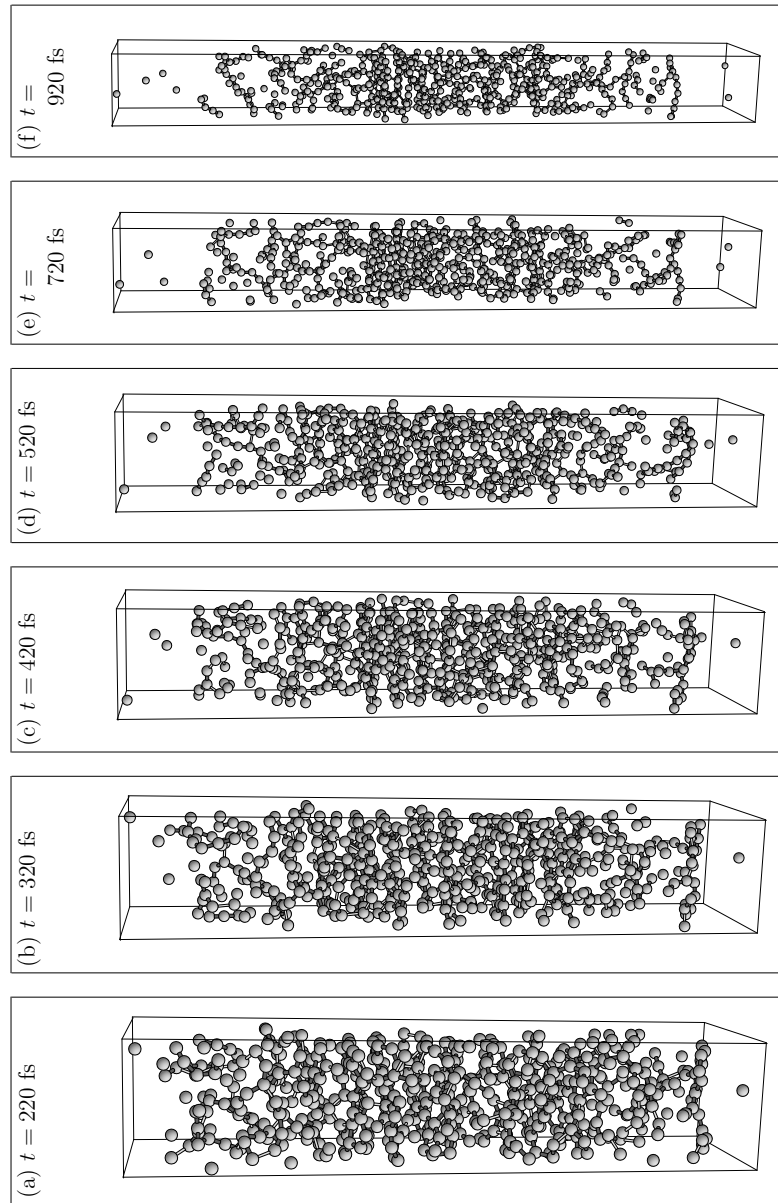


Figure 7.18: Ablation of a graphite film at an absorbed energy of $E_0 = 4.0$ eV/atom. The laser pulse duration was $\tau = 20$ fs. This figure shows the advanced stages of the ablation process (for the early stages see Fig. 7.17). Four emitted carbon monomers far from the surface are not shown. A strong expansion of the material is observed; as the film has been represented with constant height, this is apparent from the narrowing of the columns. The material is in strong, liquid-like motion. In (d)-(f), in addition to the emission of carbon monomers, linear carbon chains are formed and emitted.

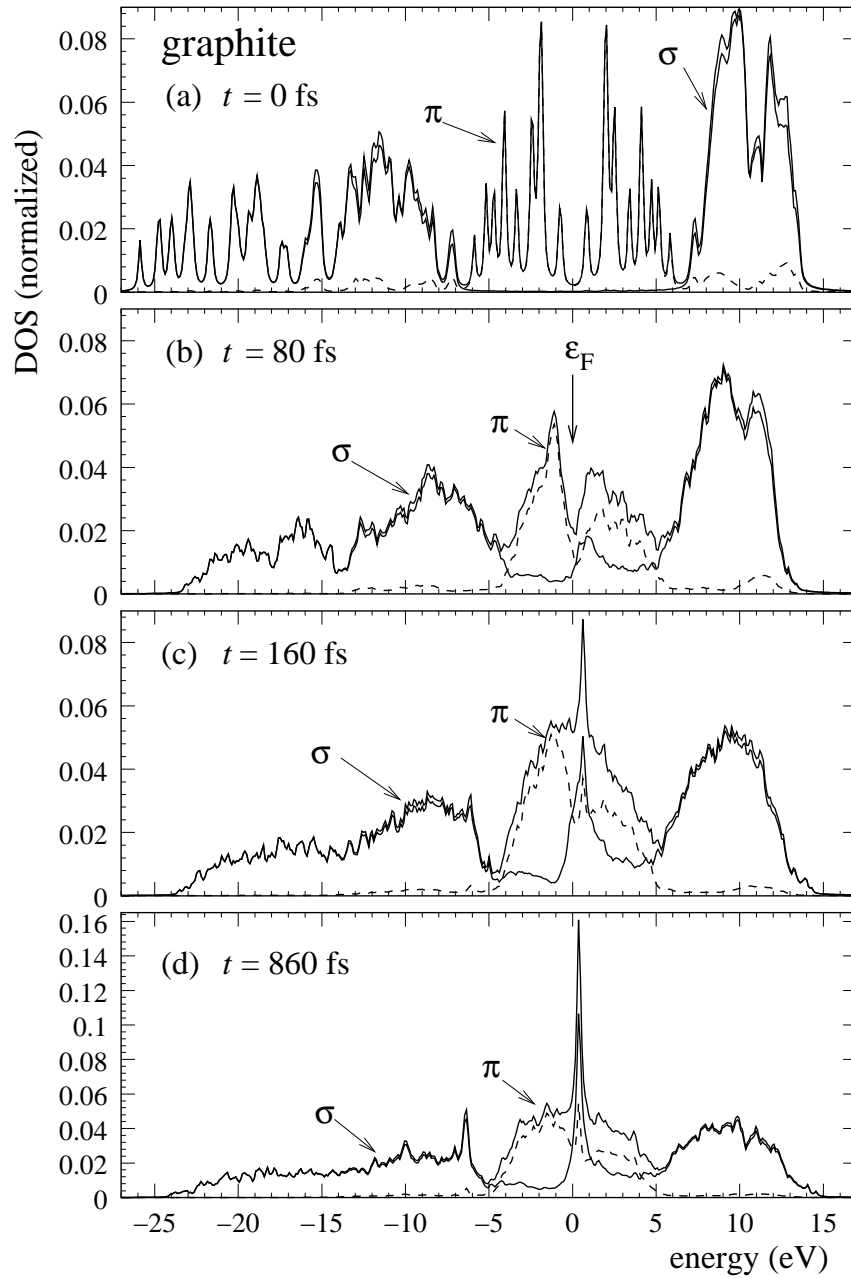


Figure 7.19: Densities of states for the ablation of graphite at an absorbed energy of $E_0 = 4.0$ eV/atom. This figure corresponds to the trajectory of Fig. 7.17. The π contribution to the DOS is indicated by a dashed line. The features of the graphite DOS in (a) at $t = 0$ fs are quickly replaced by a metallic-like DOS (b). The sharp peak at the Fermi level that appears at $t = 160$ fs in (c) is due to contributions of linear carbon chains. Note, the ordinate scale of (d) is different from (a) to (c).

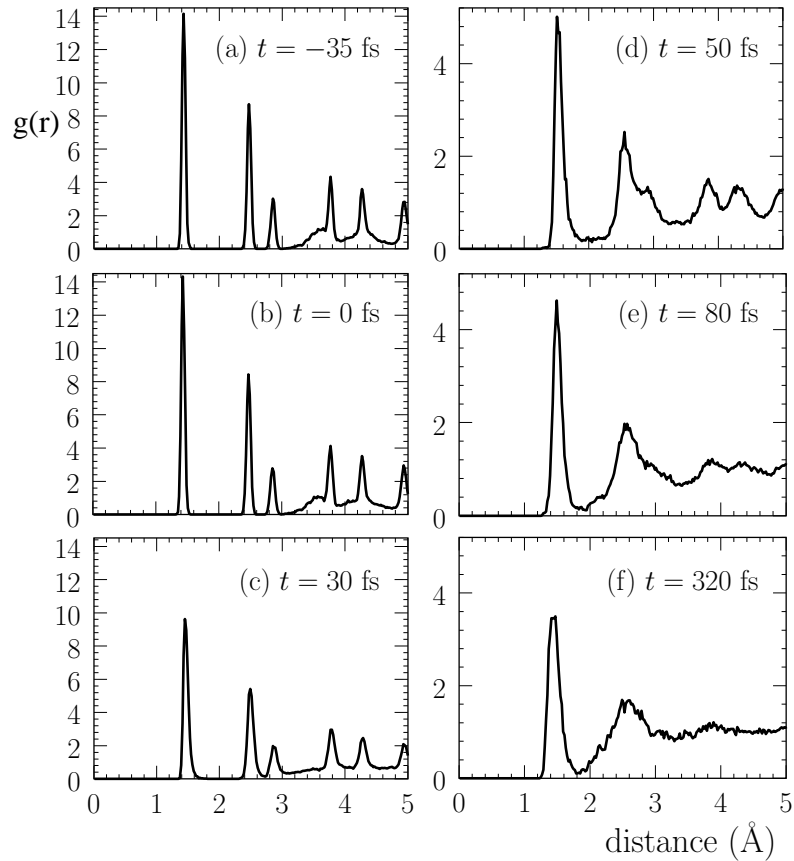


Figure 7.20: Pair correlation function $g(r)$ during the melting of a graphite film at an absorbed energy of $E_0 = 4.0$ eV/atom. The pulse duration was $\tau = 20$ fs. The time of (a) is negative because we measure time with respect to the laser pulse maximum. The pair correlation functions correspond to the same trajectory as Figs. 7.17 to 7.19. Note, the ordinate scale of the left figures is different from that on the right. At $t = 0$ fs, $g(r)$ is not significantly modified with respect to $g(r)$ before the pulse (see (a)). At $t = 30$ fs (see (c)) the structures of $g(r)$ have slightly broadened. Shortly afterwards (see (d) and (e)), the pair correlation function of liquid carbon is formed.

the same trajectory as Figs. 7.17 to 7.19. $g(r)$ at the pulse maximum (see Fig. 7.20 (b)) does not yet differ much from $g(r)$ before the pulse (Fig. 7.20 (a)). But then a rapid broadening of the structures of $g(r)$ occurs (Fig. 7.20 (c) and (d)) and at $t = 80$ fs the pair correlation function of liquid carbon is recognizable.

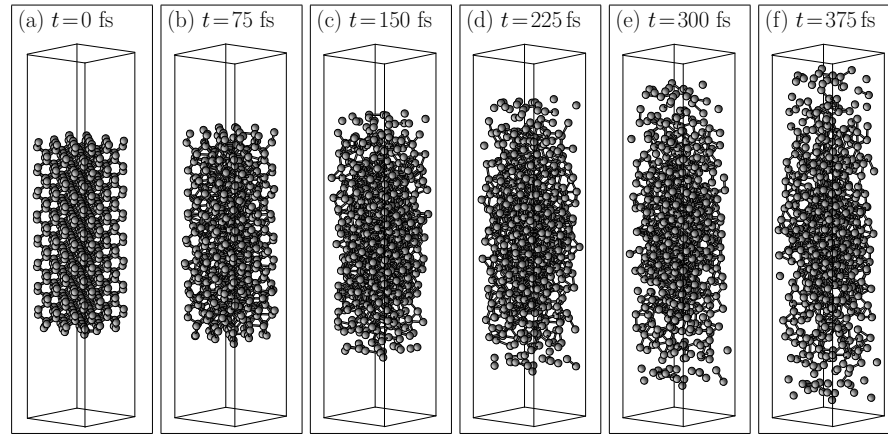


Figure 7.21: Ablation of a silicon film at an absorbed energy of $E_0 = 6.1$ eV/atom. The laser pulse duration was $\tau = 20$ fs.

6. Ablation of silicon

Silicon was among the first materials for which ultrafast structural transformations were observed [163, 164]. Its optical response following laser irradiation was studied in great detail [166]. This prompted early theoretical investigations, namely studies of the softening of phonon modes as a result of a laser induced electron hole plasma [179, 180, 181] and of the melting of the material due to a high electron temperature [184].

We have performed simulations of the laser melting and ablation of silicon in the bulk and in films. Results for the ablation thresholds from calculations in the bulk have been published elsewhere [190]. In Fig. 7.21 we show snapshots of the ablation of a (111) silicon film. The laser pulse of $\tau = 20$ fs duration had an intensity of $E_0 = 6.1$ eV/atom. This absorbed energy is far above the ablation threshold of the material. Thus, already within 75 fs after the incidence of the pulse, the lattice is strongly disordered. A fast expansion can be observed, and material is evaporating on both surfaces of the film.

In order to analyse the structural response of the material after laser irradiation, we determined the pair correlation function for the silicon film trajectory of Fig. 7.21. The results are shown in Fig. 7.22. The sharp features of the crystalline structure of silicon broaden very rapidly during the first 100 fs after the pulse, and at $t = 150$ fs, calculated from the laser pulse maximum, the pair correlation of liquid silicon is almost reached. This confirms that the melting process involves a nonthermal mechanism as thermal melting would take at least an order of magnitude longer.

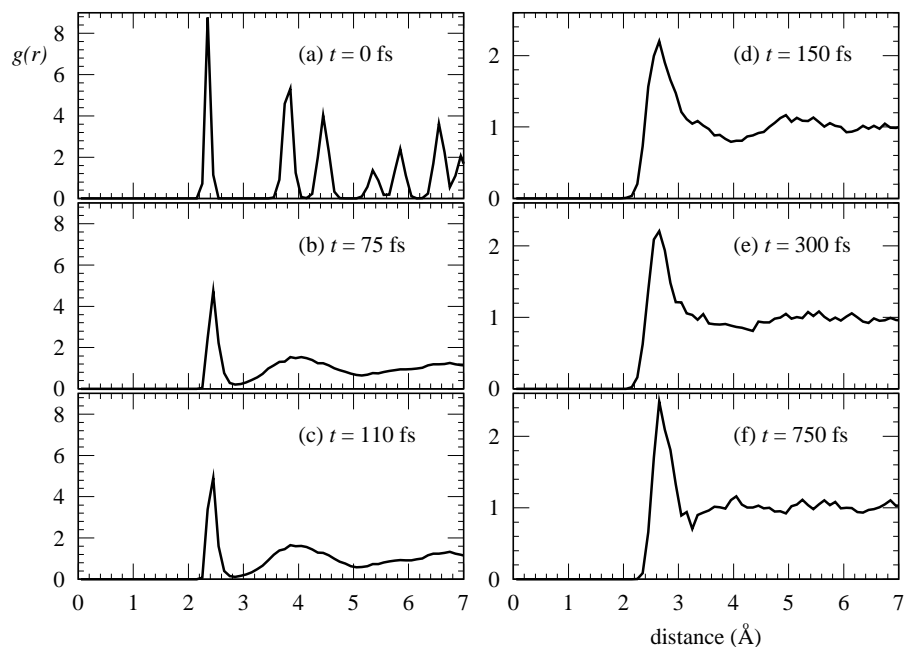


Figure 7.22: Pair correlation function $g(r)$ during the melting of a silicon film at an absorbed energy of $E_0 = 6.1$ eV/atom. The pulse duration was $\tau = 20$ fs. The pair correlation functions correspond to the same trajectory as Fig. 7.21. It was calculated for a slab 20 Å in height from the center of the film in order to exclude the surfaces of the material. Note, the ordinate scale of the left figures is different from that on the right.

7. Laserinduced melting of a C_{60} molecular crystal

The C_{60} molecular crystal is an interesting object of study as it represents a solid carbon material with a density that is app. 20% below that of graphite. Thus, it is a possible starting point for the creation of low density liquid carbon (LDLC) [216]. Laser excitation of fullerenes can also lead to polymerization and amorphization [217].

For the simulation of the ultrafast relaxation of a C_{60} molecular crystal we consider a supercell of 240 atoms and periodic boundary conditions.

In Fig. 7.23 we show snapshots of the destruction of a C_{60} molecular crystal induced by intense laser irradiation. The laser pulse is characterized by a duration of $\tau = 20$ fs, and during its action an energy of $E_0 = 3.6$ eV/atom is absorbed by the lattice. A constant external isotropic pressure of $P = 10$ GPa is applied to the system at all times. In the figure we indicate bonds up to a length of 1.6 Å with dark grey, while bonds between 1.6 Å and 2.1 Å in length are shaded in light grey and have a smaller diameter. Bonds longer than 2.1 Å are not shown, as they contribute only negligibly to the binding energy,

and thus atoms that are more than 2.1 \AA apart can be considered unbound. At $\Delta t = 0 \text{ fs}$ (Fig. 7.23 (a)), i.e. at the pulse maximum, the atoms have not yet had time to react to the change in the PES due to the absorption of nearly half of the laser intensity; they still form the perfect fcc lattice of the solid C_{60} at 300K. The fact that in each of the C_{60} molecules a few atoms seem to be missing while several atoms can be seen that are not directly connected to one of the four C_{60} molecules is a consequence of the periodic boundary conditions. The six atoms on the bottom left of the first panel for example actually form a part of the C_{60} molecule in the background. At $\Delta t = 20 \text{ fs}$ (Fig. 7.23 (b)), the C_{60} molecules have expanded considerably as can be seen from the many light grey, i.e. stretched, bonds that have replaced dark grey ones. At $\Delta t = 60 \text{ fs}$ (Fig. 7.23 (c)), the expansion of the C_{60} molecules has proceeded beyond the elastic limit of the C-C bonds, and the original form of the C_{60} molecules appears mainly in the large hollow spaces not yet filled in by the hot carbon atoms. Through the collision processes between the fragments of the C_{60} molecules, the kinetic energy of the system has now increased by 2200 K to $T_l = 2500 \text{ K}$. At $\Delta t = 160 \text{ fs}$ (Fig. 7.23 (d)), the fragments of the destroyed C_{60} molecules have filled up most of the available space, and the distribution of matter approaches homogeneity. Up to a time delay of approximately $\Delta t = 120 \text{ fs}$, the volume of the system has decreased very rapidly by 30% because the resistance of the nearly incompressible C_{60} molecules to the external pressure has vanished. The panels for $\Delta t = 260 \text{ fs}$ and $\Delta t = 860 \text{ fs}$ (Fig. 7.23 (e) and (f)) show rapid structural rearrangements of the very hot ($T_l \approx 3000 - 3500 \text{ K}$) material. The density at $\Delta t = 860 \text{ fs}$ is $\rho = 2.5 \text{ g/cm}^3$. A very long simulation of several hundred picoseconds will be needed to determine the final structure of the material after cooling through slow processes like heat diffusion. Recently, results on the laser induced melting of fullerenes have also been reported on an *ab initio* [218] and on a TB basis [216].

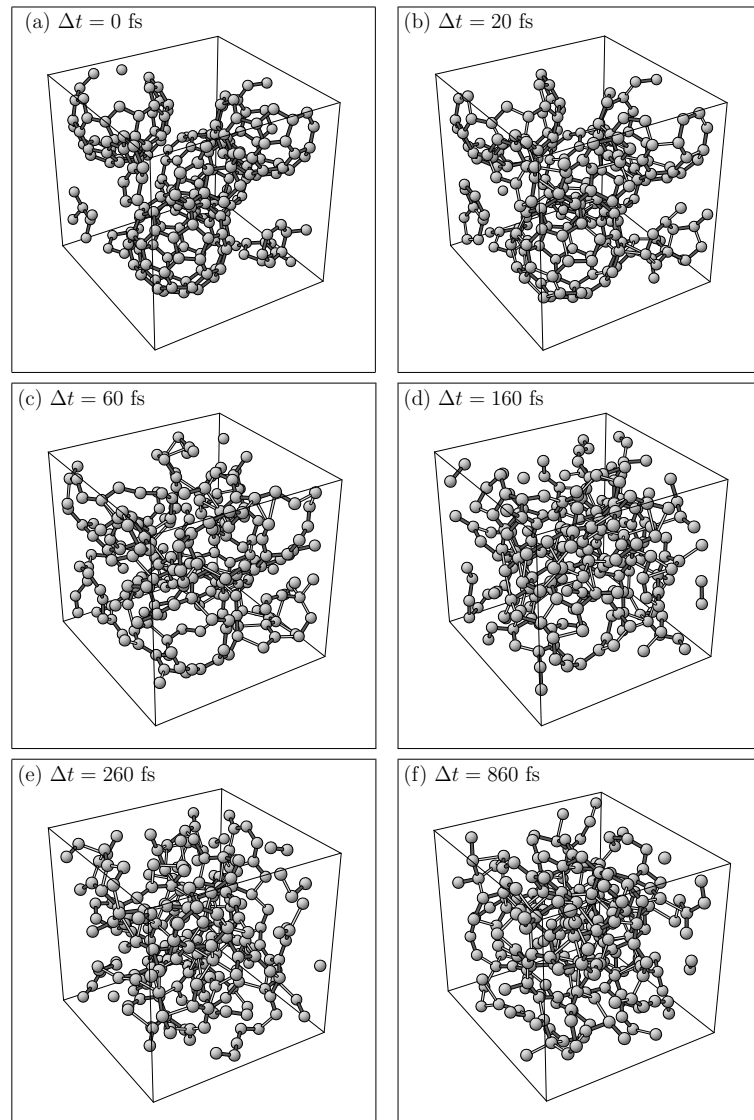


Figure 7.23: Snapshots of a C_{60} molecular crystal during and after irradiation by an ultrashort laser pulse. Pulse duration is $\tau = 20$ fs, an energy of $E_{abs} = 3.6$ eV/atom is absorbed during the laser excitation. A constant external pressure of $p = 10$ GPa acts on the crystal. Time delays Δt are given with respect to the peak of the pulse. Bonds up to a length of 1.6 Å are shown in dark grey, bonds between 1.6 Å and 2.1 Å in length are shown in light grey and are thinner in diameter. For a detailed discussion of the dynamics please refer to the text.

8. Fragmentation of nanotubes

In this section, we will analyze fragmentation mechanisms of carbon nanotubes. These materials are fascinating objects of investigation in its own right as the many different nanotube structures show diverse physical properties.

We present results for the fragmentation of two different sizes of nanotubes. The nanotubes were treated with periodical boundary conditions in the z direction. Thus, they are assumed to be infinite in length. In Fig. 7.24, we present snapshots of the fragmentation of a (10,0) nanotube. An energy of $E_0 = 2.2$ eV/atom was absorbed from a laser pulse of $\tau = 20$ fs duration. This absorbed energy is slightly above the fragmentation threshold and only a few monomers are emitted. At $t = 900$ fs after the pulse, five monomers have left the nanotube.

In Fig. 7.24, we can observe two typical damage mechanisms which have been found in all trajectories of fragmenting nanotubes. The first is the emission of monomers and the creation of a hole in the otherwise undamaged wall of the nanotube. This process takes place on the upper left hand side of the nanotube in Fig. 7.24 (b) and (c). Although the atom that can be seen to leave the nanotube in Fig. 7.24 (c) appears to be removed from the ragged edge of the tube, the mentioned periodical boundary conditions in the z direction mean that this process actually takes place on the side of a perfectly regular, infinite nanotube. From this hole a total of four carbon monomers are emitted. At $t = 900$ fs (see Fig. 7.24 (d)) a neat hole is visible.

The other typical damage creation process is taking place on the right hand side of the nanotube in Fig. 7.24. Starting at $t = 110$ fs (see Fig. 7.24 (a)) we observe the emergence of a tear in the tube. At $t = 160$ fs, one carbon monomer is emitted from this damage spot. Although no more emission of fragments is observed after that, the damage continues its development. At $t = 900$ fs (see Fig. 7.24 (d)) a group of 12 atoms has straightened out into a segment of a graphite plane. Thus, the tear in the side of the tube has caused a relaxation which lowers the surface tension which distinguishes the nanotube from an even graphite plane.

The fragmentation threshold for the (10,0) nanotube was found to be 2.01 ± 0.13 eV/atom, for the (7,0) nanotube 1.83 ± 0.14 eV/atom. Both results are for laser pulses of $\tau = 20$ fs duration. Thus, the nanotube with the smaller diameter is less stable with respect to laser excitation; the diameter of the (10,0) nanotube is $d = 7.8$ Å, of the (7,0) nanotube $d = 5.5$ Å. This can be understood as follows: The π bonds formed by the $2p_z$ orbitals of carbon in a graphite plane are affected strongly when the plane is rolled into a narrow tube. The narrower the nanotube, the lower is the overlap of the p orbitals on the outside of the tube. In other words, the (7,0) nanotube shows a higher surface tension than

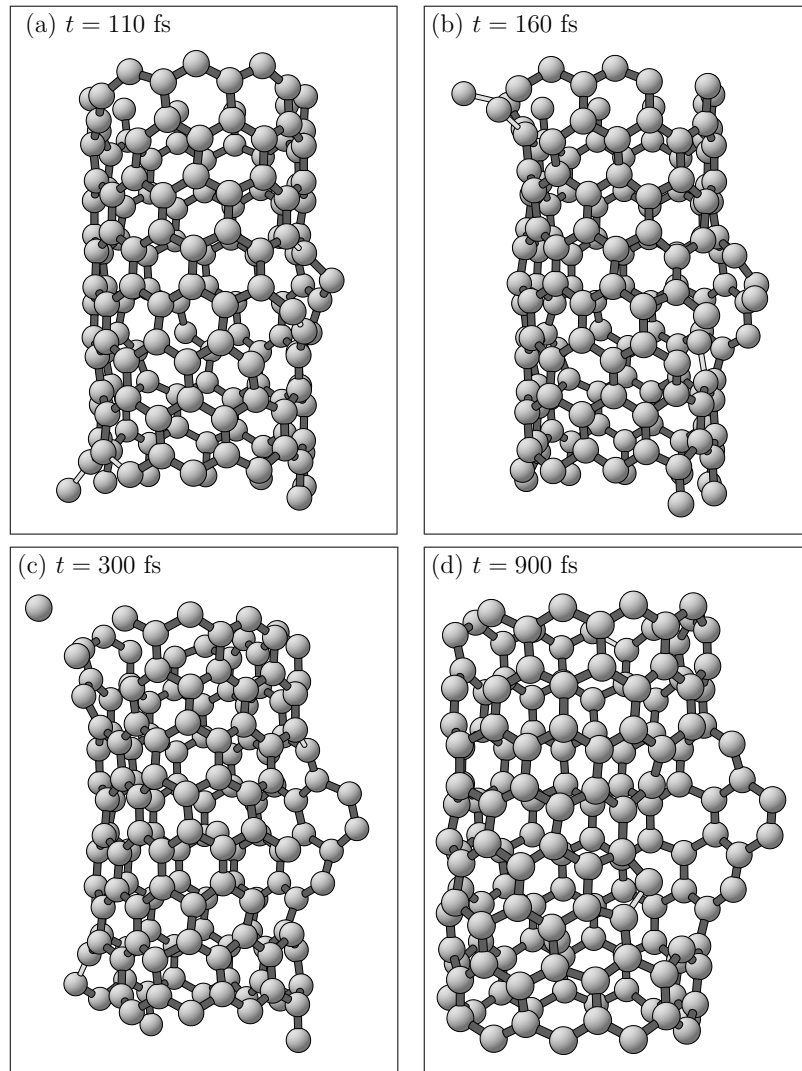


Figure 7.24: Fragmentation of a (10,0) carbon nanotube. In (c), two atoms on the left and one atom on the right of the tube that had moved far from the tube after emission have been removed; in (d), a total of five distant monomers are not shown. Note, periodic boundary conditions in the z direction have been employed, so that the edges on the top and the bottom of the nanotube segment are not present in the calculation. Two important mechanisms of damage development can be observed in this sequence: On the upper left hand side a neat hole is created via the emission of four carbon monomers. On the right hand side a tear appears and leads to a partial unfolding of a graphite plane segment.

the (10,0) nanotube, and this explains the higher vulnerability in the presence of an electron-hole plasma.

The fragmentation thresholds given here are valid for a time up to 2 ps. Thus, they refer to the nonequilibrium fragmentation. It is to be expected that also slightly below the threshold the energy deposited in the cluster can after redistribution lead to a thermal fragmentation. Consequently a threshold including nonequilibrium and equilibrium fragmentation processes would be a little lower than those given here.

9. Summary

An approach to the laser induced structural instabilities of covalent materials has been developed on the basis of a tight binding molecular dynamics (TBMD) formulation. Writing equations of motion for the occupations of the electronic levels of the system, we can study the response to the shape, intensity and colour of an ultrashort electromagnetic field interacting with the material. The time evolution of the electronic occupations leads to molecular dynamics simulations on time dependent potential energy surfaces. By applying our method in the form of constant pressure MD simulations to bulk systems or alternatively to film geometries where surface effects can be described explicitly, we make sure that we do not artificially suppress relaxation channels. Our findings can, in part, be compared to methods introducing a high electron temperature into Car-Parrinello or TBMD calculations or to methods simulating excited states in molecular dynamics calculations on an empirical pair potential basis.

We presented applications of our method to a variety of materials, focusing our attention on the microscopic processes underlying laser induced structural phase transformations. In diamond, we find that the dominant damage mechanism upon absorption of an energy of roughly 1 eV/atom from an ultrashort laser pulse is a rapid graphitization. Within approximately 200 fs of the peak of an above-threshold pulse, the density of states of the material dramatically changes its character from that of diamond to that of graphite. In the study of the ablation of graphite we find a previously unknown damage mechanism that doesn't involve the breaking of bonds in the graphite planes. Instead, strong vibrational excitation of the intact planes lead to inter-plane collisions and to the removal of entire planes through the transferral of momentum. This mechanism may be relevant in the interpretation of time dependent reflectivity measurements and for understanding the formation of carbon nanotubes. At higher deposited laser energies we describe the nonequilibrium melting of graphite which leads to a carbon phase dominated by linear carbon chains before the material evaporates. In a study of the laser melting of a silicon film we show that the development of the pair correlation function of the liquid state takes less than 200 fs, confirming that the laser induced electron hole plasma leads to a nonthermal melting

process. This observation also holds for the other materials we have studied. The interaction of an intense laser pulse with a C₆₀ molecular crystal under pressure leads to ultrafast destruction of the C₆₀ molecules and the formation of a homogeneous carbon melt. Finally, in the laser fragmentation of a carbon nanotube we can distinguish two damage processes, namely the emission of carbon monomers and the unfolding of the tube after laser induced bond breaking.